

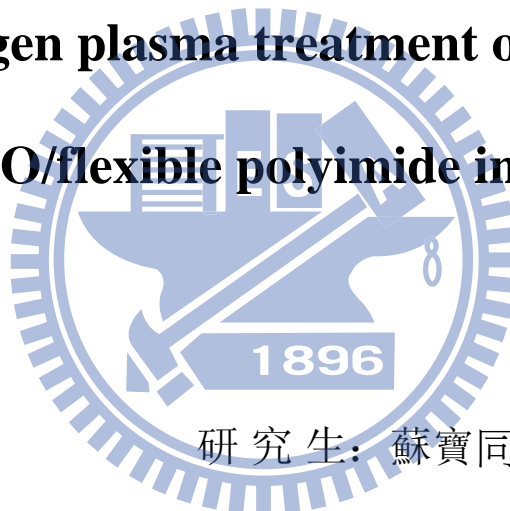
國立交通大學

材料科學與工程學系

碩士論文

Effect of oxygen plasma treatment on the adhesion of

AZO/flexible polyimide interface



研究生：蘇寶同

指導教授：呂志鵬 教授

中華民國九十九年十一月

Effect of oxygen plasma treatment on the adhesion of AZO/flexible polyimide interface

研究生：蘇寶童

Student: To Bao Dong

指導教授：呂志鵬 教授

Advisor: Dr. Jihperng (Jim) Leu

國立交通大學

材料科學與工程學系

碩士論文

The logo of National Chiao Tung University is a circular emblem with a gear-like outer border. Inside the circle, there is a stylized building and the acronym 'NCTU'. The year '1896' is prominently displayed at the bottom of the inner circle.

A Thesis
Submitted to Department of Materials Science and Engineering
College of Engineering
National Chiao Tung University
1896
In partial Fulfillment of the Requirements
for the Degree of
Master

in

Materials Science and Engineering

November 25, 2010

Hsinchu, Taiwan, Republic of China

Effect of oxygen plasma treatment on the adhesion of AZO/flexible polyimide interface

Student : Bao Dong To

Advisor: Dr. Jihperng (Jim) Leu

Department of Materials Science and Engineering

National Chiao Tung University

Abstract

This study focuses on using oxygen plasma treatment to improve the adhesion between ODPB-BADB polyimide (PI) and aluminum-doped zinc oxide (AZO). The results from this research can be applied to flexible devices such as FOLED or flexible solar cell. A new ODPB-BADB polyimide was synthesized in this research group by using two monomers 4,4'-oxydiphthalic anhydride (ODPA) and bis(4-aminophenyl)-1,4-diiisopropylbenzene (BADB). ODPB-BADB polyimide film possesses high glass transition temperature ($T_g = 252\text{ }^\circ\text{C}$) and high transmittance (90%). The effect of oxygen plasma treatment conditions (power and treatment time) on the adhesion characteristics of polyimide surface and AZO/PI interface were investigated by means of four-point bending test method, contact angle measurement, X-ray photoelectron spectroscopy (XPS), and atomic force microscopy (AFM). The effect of oxygen plasma treatment to on electrical properties and surface energies of AZO films also investigated by four-point probe and X-ray diffraction (XRD). The results showed that both the surface energy of PI and adhesion energy of AZO/PI increased significantly after PI was treated by oxygen plasma. Adhesion energy increased with the increasing of RF treatment power, but the surface energy of PI increased only

slightly with increasing RF power and treatment time. The enhanced adhesion at AZO/PI interface could be attributed to increased roughness, the formation of the new polar group such as C-OH and increased percentage of oxygenated, polar groups such as C-O and C=O on PI surface. The surface of AZO remained very smooth when deposited onto oxygen plasma-modified polyimide films. However, the resistivity of AZO film was degraded when the polyimide film was treated by oxygen plasma. The increased resistivity of AZO films can be attributed to the increased surface roughness of polyimide by plasma modification and possibly the incorporation of C and O impurities during sputtering deposition.



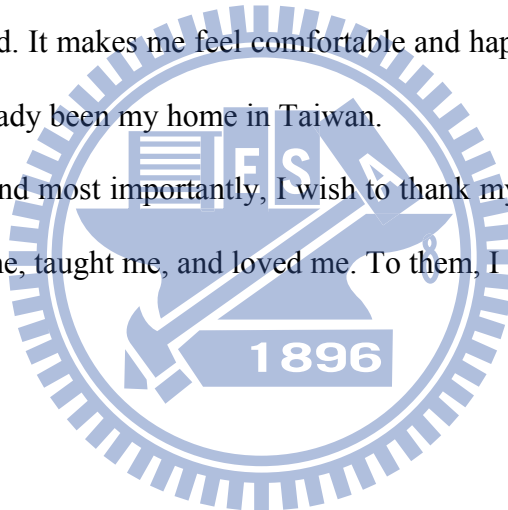
Acknowledgements

I would like to express my deep and sincere gratitude to my advisor, Dr. Jihperng (Jim) Leu for his expertise, understanding, patience, and greatest consideration to my entire study.

I wish to thank Dang Van Thanh, Do Thi Hien, Lam Tu Ngoc, who gave me a lot of help in my experiments.

During the time study in Taiwan, I am very grateful to be the members of Nano-Interconnect & Package Laboratory (NIPL). All of people in our lab are always friendly and kind. It makes me feel comfortable and happy to be one of NIP members. NIP lab has already been my home in Taiwan.

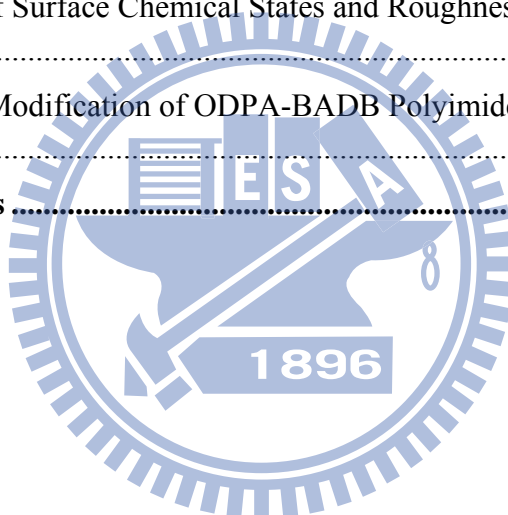
Lastly, and most importantly, I wish to thank my parents, they born me, raised me, supported me, taught me, and loved me. To them, I dedicate this thesis.



Contents

Abstract	iii
Acknowledgements	v
List of Tables	viii
List of Figures	x
Chapter 1 Introduction	1
1.1 General Background	1
1.2 Outline of The Thesis.....	3
Chapter 2 Literature Review	5
2.1 Introduction of Flexible Devices	5
2.1.1. Several Popular Materials Provide Flexible Substrate.....	7
2.1.2 Material Challenge of the Flexible Substrate in the Flexible Devices.....	9
2.2 Analysis of the Adhesion Strength.	12
2.3 Plasma Surface Modification to Improve the Reliability of Flexible Devices.....	14
2.4 Transparent Conductors	17
2.5 Effect of Oxygen Plasma Treatment on the Electrical Properties	19
Chapter 3. Experimental Procedures	21
3.1 Sample Preparation	21
3.1.1 Synthesis of ODP A-BADB polyimide	21
3.1.3 Deposition of Aluminum-Doped Zinc Oxide (AZO) Film.....	23
3.1.4 Measurement Procedure and Data Analysis for Four Point Bending Adhesion Test.....	24
3.2 Experimental Method and Procedures	28
3.3 Introduction of Instruments.....	30
3.3.1 Reactive Ionic Etching (RIE).....	30
3.3.2 X-ray Photoelectron Spectroscopy (XPS)	30
3.3.3 Curve Fitting XPS Data	34
3.3.4 Atomic Force Microscope (AFM)	36
3.3.5 Contact Angle Measurement.....	38
3.3.6 Scanning Electron Microscopy (SEM)	39
3.3.7 Physical-Vapor Deposition	40
3.3.8 Four Point Bending System	41
3.3.9 Four Point Probe System	42

3.3.10 X-ray Diffraction (XRD)	43
Chapter 4 Results and Discussion.....	44
4.1 XPS Analysis of Surface Chemical States of ODPA-BADB Polyimide.....	45
4.3 Surface Energy of ODPA-BADB Polyimide.....	64
4.4 Adhesion of AZO/PI Interface.....	67
4.5 Surface Roughness of AZO/PI Using AFM	71
4.6 XRD of AZO Film Deposited on Polyimide	74
4.7 Resistivity of AZO Deposited on Polyimide	76
4.8 Discussion.....	77
4.8.1 Modification of ODPA-BADB Polyimide Surface Chemical State.....	77
4.8.2 Surface Chemical States Affect on Surface Energy of ODPA-BADB Polyimide	80
4.5.3 Effects of Surface Chemical States and Roughness on the Adhesion of AZO/PI Interface	82
4.5.6 Surface Modification of ODPA-BADB Polyimide Affect on Electrical Property of AZO	83
Chapter 5 Conclusions	84



List of Tables

Table 2. 1.	Properties of typical polymeric films as plastic substrates.....	11
Table 2. 2.	XPS binding energies and relative peak areas of deconvoluted C 1s spectra obtained from 6FDA-BisAAF fluorinated polyimide before and after different plasma treatment.....	16
Table 2. 3.	Values of the pull strength, surface roughness, and increased chemical states in samples.	16
Table 2. 4.	TCO materials for thin-film transparent electrodes.....	18
Table 2. 5.	Comparison of thin-film transparent electrode properties between AZO and ITO films.....	18
Table 3. 1.	Chemical structures and molecular weights of monomers and solvent.....	22
Table 3. 2.	Plasma treatment conditions of ODPA-BADB polyimide film	23
Table 3.3.	Deposition parameters for AZO film on PI.....	24
Table 4. 1.	Main components and their binding energies fitting in C 1s and O 1s XPS signals of ODPA-BADB polyimide	47
Table 4. 2.	Carbon 1s spectrum: binding energies and composition quantification of untreated ODPA-BADB polyimide film.....	48
Table 4. 3.	Carbon 1s spectrum: binding energies and composition quantification of ODPA-BADB polyimide film modified by oxygen plasma at 50W RF Power, time treatment for 1min	48
Table 4. 4.	Carbon 1s spectrum: binding energies and composition quantification of ODPA-BADB polyimide film modified by oxygen plasma at 50W RF Power, time treatment for 5 min	49
Table 4. 5.	Carbon 1s spectrum: binding energies and composition quantification of ODPA-BADB polyimide film modified by oxygen plasma at 100W RF Power, time treatment for 5min	50
Table 4. 6.	Oxygen 1s spectrum: binding energies and composition quantification of untreated ODPA-BADB polyimide film	54
Table 4. 7.	Oxygen 1s spectrum: binding energies and composition quantification of ODPA-BADB polyimide film modified by oxygen plasma at 50W RF Power, time treatment for 1min	55
Table 4. 8.	Carbon 1s spectrum: binding energies and composition quantification of ODPA-BADB polyimide film modified by oxygen plasma at 50W RF Power, time treatment for 5 mins.....	55
Table 4. 9.	Oxygen 1s spectrum: binding energies and composition quantification of ODPA-BADB polyimide film modified by oxygen plasma at 100W RF Power, time treatment for 5 mins.....	56
Table 4. 10.	The contact angle, wetting tension, and surface energy of PI surface with and without oxygen plasma treatment (raw data)	65

Table 4. 11.	The surface energy of PI surface with and without oxygen plasma treatment	66
Table 4. 12.	The critical loads and adhesion strength of AZO/PI interface for PI with and without oxygen plasma treatment with different RF power.	70
Table 4. 13.	The average values of adhesion energy AZO/PI interface for PI with and without oxygen plasma treatment.....	70
Table 4. 14.	The average grain size of AZO deposited on untreated PI and oxygen plasma modified PI.	75
Table 4. 15.	Resistivity of AZO thin films deposited on polyimide films with and without oxygen plasma modification.....	76
Table 4. 16.	Binding energies of typical chemical bonds.	79
Table 4. 17.	Binding energies (eV) and composition quantification (%) of ODPA-BADB polyimide as obtained by XPS C1s and O1s spectra.....	80



List of Figures

Figure 2. 1.	Flexible Display Technology and Market (2007~2017) report	6
Figure 2. 2	. Photograph of the OTFT-driven OLED display under operation	7
Figure 2. 3.	Device configuration of a flexible surface-emitting OLED with a steel foil substrate.	8
Figure 2. 4.	Schematic multilayer structure of an encapsulated OLED.	9
Figure 2. 5.	The structure of the flexible a-Si solar cell	9
Figure 2.6.	WVTR requirements for common flexible electronic devices and the barrier performance by available materials.	11
Figure 2. 7.	Primary failure modes for brittle films on the polymer substrates.....	12
Figure 2. 8	Three fracture modes: (a) mode I, (b) mode II, and (c) mode III	14
Figure 2. 9.	The common techniques for measuring the interfacial strength	14
Figure 2. 10.	XRD patterns of AZO thin films deposited on (a) PES (b) PET and (c) FQ substrates.	20
Figure 3. 1.	Synthesis reaction of ODPA-BADB polyimide.....	22
Figure 3.2.	Sample preparation steps for four point bending test.....	26
Figure 3. 3.	C-clamp and small clamps for fixing four point bending sample.....	27
Figure 3. 4.	The stacking structure of sandwich sample and schematic drawing of four point bending test sample	27
Figure 3.5.	A typical load and displacement curve for four point bending test	27
Figure 3. 6.	Flow – chart of experimental procedures and characterization	29
Figure 3. 7.	The principle of reactive ionic etching.....	30
Figure 3. 10.	The XPS peak fitting program	35
Figure 3. 11.	AFM – schematic principle	36
Figure 3. 12.	Schematic diagram of a contact angle measurement system	38
Figure 3. 17.	Arrangement of a four-point probe on a rectangular sample	43
Figure 3. 18.	Definition of the angle of incidence and diffraction in an XRD experiment.....	44
Figure 4. 1.	Binding states of the (a) carbon and (b) oxygen atoms in the repeating unit of ODPA-BADB polyimide	47
Figure 4. 2.	The XPS C 1s spectra of untreated ODPA-BADB polyimide films.....	51
Figure 4. 3.	The XPS C 1s spectra of ODPA-BADB polyimide films oxygen plasma treated at 50W RF Power, time treatment for 1min	52
Figure 4. 4.	The XPS C 1s spectra of ODPA-BADB polyimide films oxygen plasma treated at 50W RF Power, time treatment for 5 mins	53
Figure 4. 5.	The XPS C 1s spectra of ODPA-BADB polyimide films oxygen plasma treated at 100W RF Power, time treatment for 5 mins	54
Figure 4. 6.	The XPS C 1s spectra of untreated ODPA-BADB polyimide films.....	57
Figure 4. 7.	The XPS O1s spectra of ODPA-BADB polyimide films oxygen plasma treated at 50W RF Power, time treatment for 1min	58
Figure 4. 8.	The XPS O1s spectra of ODPA-BADB polyimide films oxygen plasma treated at 50W RF Power, time treatment for 5mins	59
Figure 4. 9.	The XPS O1s spectra of ODPA-BADB polyimide films oxygen plasma treated at 100W RF Power, time treatment for 5mins	60

Figure 4. 10. The AFM two-dimensional images of the surface PI (a) the untreated, (b) 50 W RF power treated, (c) 100W RF power treated	62
Figure 4. 11. The AFM three-dimensional images of the surface PI (a) the untreated, (b) 50 W RF power treated, (c) 100W RF power treated	63
Figure 4. 12. The images of contact angle (a) untreated and (b) oxygen plasma treated PI surface	64
Figure 4. 13. SEM image for thickness of AZO deposit on polyimide.....	67
Figure 4. 14. Load – displacement graph of AZO/PI sample under four point bending test ..	69
Figure 4. 15. Surface morphology of polyimide and AZO after delamination of four point bending test	69
Figure 4. 16. The AFM two-dimensional images of AZO surfaces deposited on polyimide (a) untreated, (b) 50W RF power treated, (c) 100w RF power treated.....	72
Figure 4. 17. The AFM three-dimension images of AZO surfaces deposited on polyimide (a) untreated, (b) 50W RF power treated, (c) 100w RF power treated.....	73
Figure 4. 18. XRD patterns of AZO thin films deposited on (a) untreated PI (b) 50W for 1 minutes treated PI (c) 50 W for 5 minutes treated PI and (d) 100W for 5 minutes treated PI	75
Figure 4. 19. Proposed surface reaction mechanisms in ODPa-BADB polyimide surface were modified by oxygen plasma treatment.....	80
Figure 4. 20. Surface energy of PI films untreated and oxygen plasma treated for various times at a power of 50W.....	81
Figure 4. 21. Surface energy on PI and adhesion energy of AZO/PI interface for PI films untreated and oxygen plasma treated using different power at a fixed 5-min treatment time.....	82

Chapter 1 Introduction

1.1 General Background

Conducting transparent oxide thin films deposited on rigid glass substrates have been widely used as transparent conducting electrodes in many optoelectronic and electro-optic devices such as solar cells and organic light emitting diode devices. They have some good properties such as high optical transparency and electrical conductivity, low oxygen permeability and water vapor permeability [1]. However, glass substrate is too brittle and heavy, unsuitable for certain applications such as cellular phones, ID cards, electronic maps, and portable computers. Replacing the glass substrate with polymer materials makes possible the fabrication of lightweight, thin, and low cost, flexible devices possible using roll-to-roll processing or printing technology. For these reasons, there is strong interest in flexible devices to meet the various design and power needs of modern gadgets [2,3]. Polymer materials offer many attractive features, they also oblige limitations and challenges such as the high coefficient of thermal expansion (CTE), low glass transition temperature (T_g), low processing temperatures, high O_2 and water vapor transmission, doubtful adhesive strength in multiple layer and device degradation [4,5].

In the last few decades, indium tin oxide (ITO) thin film has been the main material used as the transparent electrodes. However, it has some disadvantage such as

toxic and high cost. Thus, Al-doped ZnO (AZO) thin films attract intensive research and development to replace ITO thin films due to its non-toxic, low oxygen vacancy, and resource availability [6,7]. Yet, one of the challenges for AZO films is the poor adhesion at AZO/polymer interface, which may result in delamination or catastrophic failure in the flexible multi-layered structure during the fabrication or in the product usage. Therefore, it is critical to enhance the adhesion of AZO film onto the polymer substrate for flexible device applications. Another technical challenge is how to fabricate crystalline AZO thin films at a sufficiently high temperature, but still below the T_g of polymer substrate. This prompts the academia and industry to develop high T_g (200-350 °C), transparent polyimide (PI) films for their excellent thermal stability, high optical transmittance of 90 % in the visible range.

Control of surface properties is very important for the high performance of adhesion in order to improve the lifetime and reliability of flexible devices. Surface modification can be achieved by a wet, dry or radiation treatment [8]. Among these methods, reactive ion etching is a plasma-based dry etching technique characterized by a combination of physical sputtering with the chemical activity of reactive species. Recently, plasma treatment has received a great attention for applications of modifying polymer surface and interface [9]. It is believed that the surface functional properties of polymer materials, which can be tailored via chemical reactions (oxygen,

fluorine, nitrogen, etc.) with polymer surface [10], are essential for controlling the surface properties and possibly interfacial adhesion as well. In this study, we investigated the effects of oxygen plasma treatment on the surface properties of PI films using the reactive ionic etching (RIE) method. Specifically, the influence of the surface properties on the adhesion strength of the PI and AZO/PI films was studied. The effects of oxygen plasma treatment on the electrical properties of AZO films and AZO surface roughness was also investigated and discussed.

1.2 Outline of the Thesis

This thesis is divided into five chapters. The contents in each chapter are described as follows:

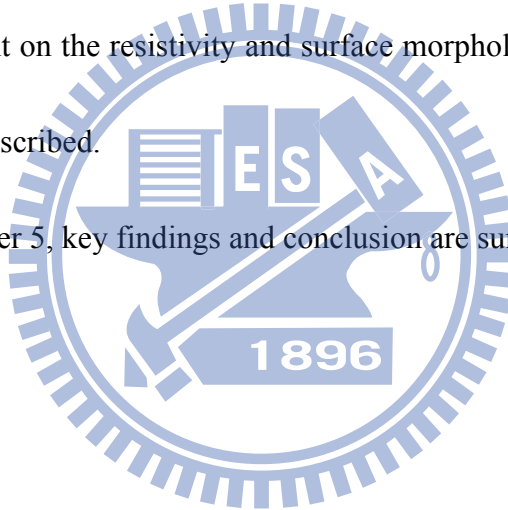
Chapter 1 introduces the general background on the applications of polymer substrates in the flexible devices, the motivations, and the organization of this thesis.

Chapter 2 reviews the literatures of flexible devices, their technological advantages, the measurement and analysis of the adhesion strength, and methods to improve the adhesion properties of the flexible devices. The transparent conductors are also reviewed, with a focus on the effects of oxygen plasma treatment of polymer substrate and the impact on the electrical properties of the subsequently deposited transparent conductors.

Chapter 3 describes the experiment method, sample preparation, and the analytic techniques.

Chapter 4 describes the results and discussions about the surface modification of polyimide films by oxygen plasma treatment. The surface chemical state, surface roughness, and surface energy of ODPA-BADB polyimide are presented. The correlation among the surface modification, the surface energy, and interfacial adhesion strength of PI/AZO are examined and proposed. The effects of oxygen plasma treatment on the resistivity and surface morphology of subsequently deposited AZO are also described.

In Chapter 5, key findings and conclusion are summarized.



Chapter 2 Literature Review

2.1 Introduction of Flexible Devices

Nowadays, with the advantage of technology, the size of electronic instruments, such as notebook computer, cellular phones, personal digital assistant (PDA), wall-mounted large screen video displays, and personal entertainment devices like MP3 player, has been constantly getting smaller, lighter and thinner and more flexible [11]. Therefore, flexible devices foster the development of a manufacturing ecosystem to support its rapidly growing market. The flexible display market value is predicted to surge from \$280 million in 2010 to \$5.9 billion in 2015, and \$12.2 billion by 2017 as shown in Figure 2.1 [12]. Clearly, flexible packaging, having developed from simple wraps and bags to more complex products with sophisticated functionality, has been one of the fastest growing sectors of the packaging market over the last decade. . For example, figure 2.2 shows the photograph of the OTFT-driven flexible OLED display and its specification [13]. Among various flexible substrates (stainless steel foil, ultrathin glass sheet, and polymer thin films), polymer substrates had received more attention because of its low cost, excellent optical characteristic, and easier production based on roll-to-roll technology. Unfortunately, flexible polymer substrates have a low ability to prevent moisture and oxygen from passing though [14]. Moreover, organic

material is sensitive to moisture and oxygen in the ambient air. Preventing the degradation of organic material caused by oxygen and moisture is essential.

Furthermore, polymer substrates have some disadvantages such as low processing temperature, poor thermal stability and reliability, and low adhesion strength with other adjacent layers due to their dissimilar material properties. These factors will affect the reliability and reduce the lifetime of flexible devices. Therefore, the reliability and mechanical integrity of the multilayered structure in the flexible devices are critical issues for the development of novel flexible devices

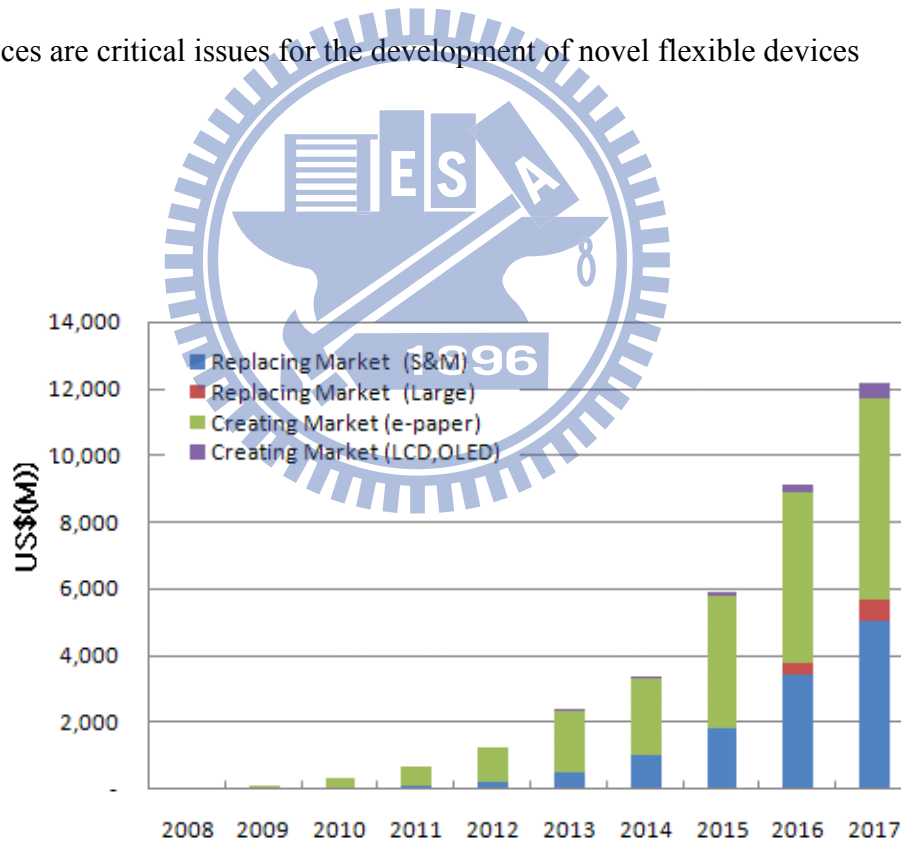


Figure 2. 1. Flexible Display Technology and Market (2007~2017) report



Figure 2. 2. Photograph of the OTFT-driven OLED display under operation

2.1.1. Several Popular Materials Provide Flexible Substrate.

Glass has been widely used as the substrate in the optoelectronic devices because glass has good chemical inertness and mechanical strength. However, there are some disadvantage in using glass because of its brittleness, inflexibility, and weight. Therefore, flexible substrates have been fervently explored to replace the glass substrate. Metal foil, flexible glass, and a variety of polymer films have been considered as the possible substrate choices for the flexible devices.

Metal foils have excellent properties such as durability and physical properties such as resistance to scratches, dings, and dents. They also possess good thermal

stability and are not permeated to water and oxygen. Some of the primary disadvantages include its high cost, difficulty in fabricating, and the heavy weight when big size products are considered. A flexible OLED fabricated on a steel foil is illustrated in Figure 2.3 [15]

Both of ultrathin glass and polymers can be used as a flexible substrate.

Polymers can sustain far greater strains than glass and hence are very flexible, but their drawback is the comparatively high rate of moisture and oxygen diffusion [16].

Ultrathin glass is a good barrier material but is brittle, which can only sustain small strain. The multilayer structure of an encapsulated OLED is shown in Figure 2.4 using an ultrathin glass [17]. In addition, the structure of the flexible a-Si solar cell polyimide substrate [18] is shown in Figure 2.5

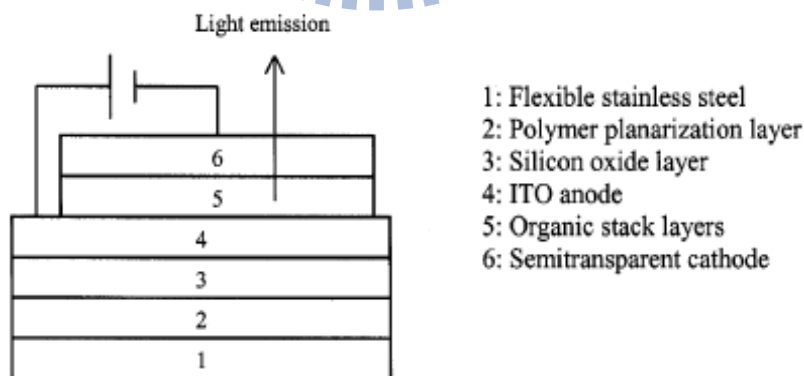


Figure 2. 3. Device configuration of a flexible surface-emitting OLED with a steel foil substrate.

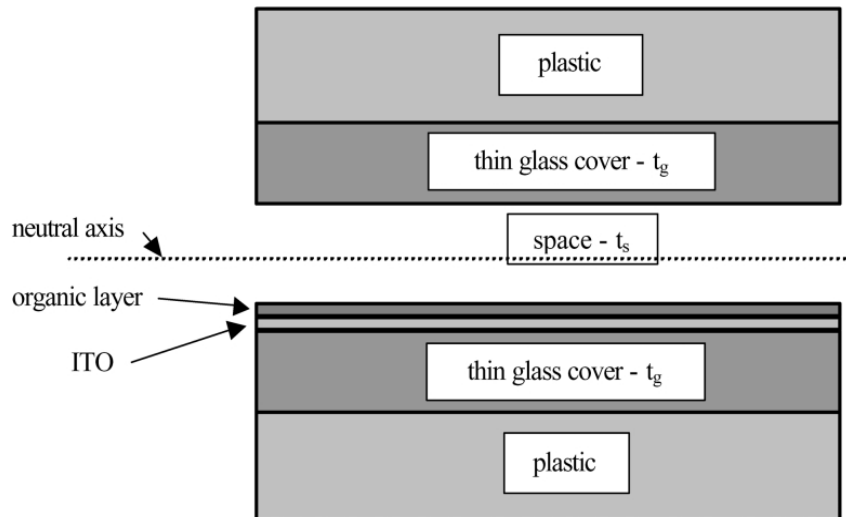


Figure 2. 4. Schematic multilayer structure of an encapsulated OLED.

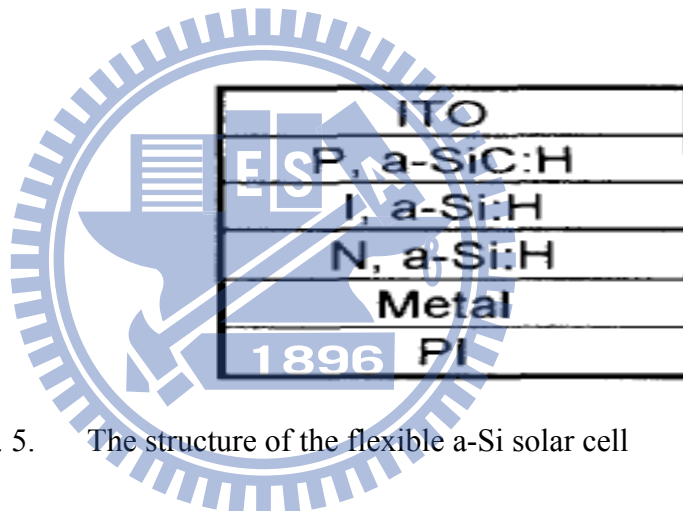


Figure 2. 5. The structure of the flexible a-Si solar cell

2.1.2 Material Challenge of the Flexible Substrate in the Flexible Devices.

First, the difficulty in developing suitable permeation barriers on polymer substrates is discussed. Figure 2.6 shows the order of magnitude of moisture protection required for various organic electronic devices and the capability provided by various materials [19]. Table 2.1 shows the optical, thermal, mechanical, and moisture barrier properties of typical polymeric films suitable as a flexible substrate [20]. Combining the data in Figure 2.6 and Table 2.1, we can see the water vapor

transmission rates (WVTR) of polymers are much higher than the required specifications. This affects the lifetime of flexible devices [21]. The life time of flexible OLED device above 10000 hours requires water vapor transmission and oxygen transmission of about $10^{-6} \text{ g m}^{-2} \text{ day}^{-1}$ and $10^{-3} \text{ cm}^3 \text{ m}^{-2} \text{ day}^{-1} \text{ atm}^{-1}$, respectively [22].

Second, the limited mechanical ruggedness of brittle inorganic films such as glass is of concern for flexible device applications. Mechanical failure in a device occurs typically at the weakest component or its interface. For inorganic thin films, these layers are normally brittle and easy failure in the flexible device under stress. [23] The details of the fracture mode depend on the Poisson's ratio of substrate, adhesion strength and cohesion of the components next to the substrate. Figure 2.7 illustrates the primary failure modes for brittle films on polymer substrates [24]. The most common failure modes for brittle films on flexible substrates are the film cracking, channeling, and debonding .

In addition, on the the requirements on the thermal properties, polymer substrate has a coefficient of thermal expansion (CTE) much higher than inorganic material. Large thermal stress was induced in the multi-layered structure upon thermal cycling due to their CTE mismatch in thermal expansion. Moreover, polymer often has low glass transition temperature, which constrains the processing temperature of

subsequent layers such as conducting transparent oxide. Polyimide in particular has received most attention due to excellent thermal stability and mechanical strength.

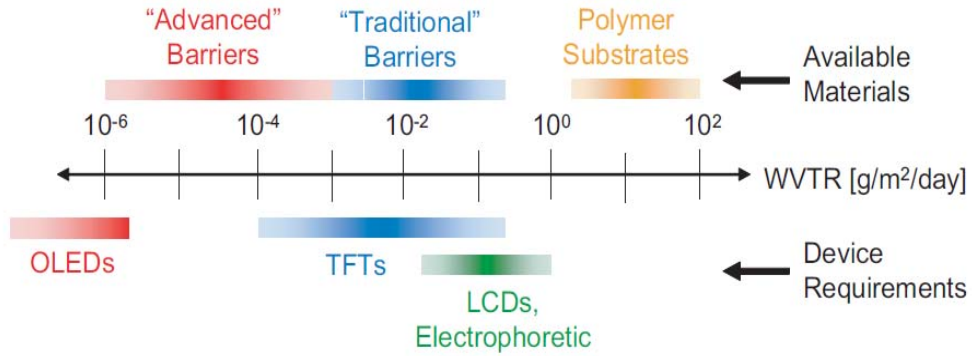


Figure 2.6. WVTR requirements for common flexible electronic devices and the barrier performance by available materials.

Table 2. 1. Properties of typical polymeric films as plastic substrates

	PET	PEN	PC	COC	PES	PI
Thickness (mm)	0.1	0.1	0.1	0.1	0.1	0.1
Total light transmittance (%)	90.4	87.0	92.0	94.5	89.0	30–60
Retardation (nm)	Large	Large	20	7	<10	Large
Refractive index	1.66	1.75	1.59	1.51	1.6	—
Glass transition temperature (°C)	80	150	145	164	223	300 <
Coefficient of thermal expansion (ppm/°C)	33	20	75	70	54	8–20
Water absorption ratio (%)	0.5	0.4	0.2	<0.2	1.4	2.0–3.0
H ₂ O barrier (g m ⁻² day ⁻¹)	9	2	50	—	80	—

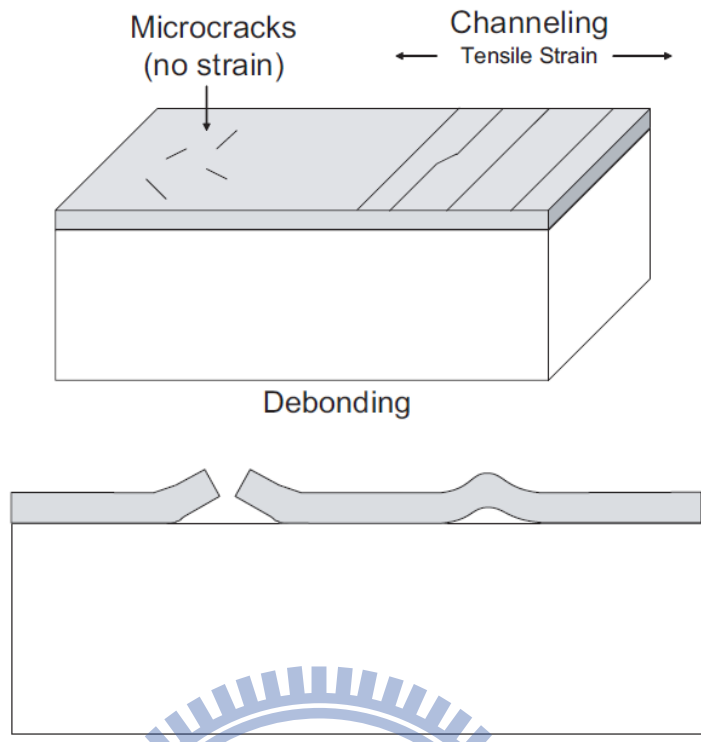


Figure 2. 7. Primary failure modes for brittle films on the polymer substrates

2.2 Analysis of the Adhesion Strength.

Many types of mechanical deformation geometries can be used to study thin film interface strength. All of test methods derive the interface strength by measuring a critical property and theoretical calculation. As the sample is tested by applying loading, fracture begins when the load increases over the critical adhesive or cohesive strength. Some common test methods including scratch test [25], Scotch tape™ test [26], and stud pull [27] are shown in Figure 2.9. However, the Scotch tape™ test cannot measure a quantitative values, and scratch test that could not measure the true adhesion at the interface. Thus, the scratch and Scotch tape™ test methods are not

suitable for quantitatively measuring the interfacial adhesion. In contrast, four-point bending, edge-lift-off, and nanoindentation tests [28] developed in the last decade offer quantitative measurement of adhesion

There are three ways of applying a force to enable a crack to propagate as shown in Figure 2.8, including tensile mode (mode I), in-plane shearing mode (mode II), and tearing mode (mode III) [29]. A tensile stress is normal to the plane of the crack in mode I, while a shear stress acts parallel to the plane of the crack and perpendicular to the crack front in mode II. Mode III is a mixed mode of tensile load of mode I and shear loading of mode II. The test system for mode II can load in two dimensional plane with the fracture phase angle ranges from 0° to 90°.

Among these adhesion tests, four-point bending test is the best choice as the technique to determine the interfacial adhesive strength because it has at least two advantages. It can quantify the exactly fracture energy, and it is a mode III, which is a fixed fracture mode with a fracture phase angle, $\Psi \sim 43^\circ$ [30]. The interfacial adhesion strength is commonly characterized by the critical energy release rate (G_c). Four-point bending test can give quantitative G_c , whereby the results obtained are reproducible. It is well established that G is a function of phase angle of mixed-mode stress intensity as defined by Eq. (2.1) [31]

$$\Psi = \arctg(K_{II}/K_I) \quad (2.1)$$

Where K_I and K_{II} denote the Mode I and Mode II stress intensity factors

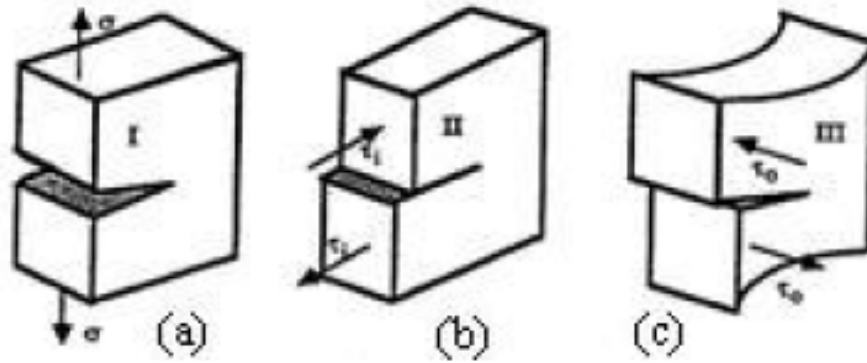


Figure 2. 8 Three fracture modes: (a) mode I, (b) mode II, and (c) mode III

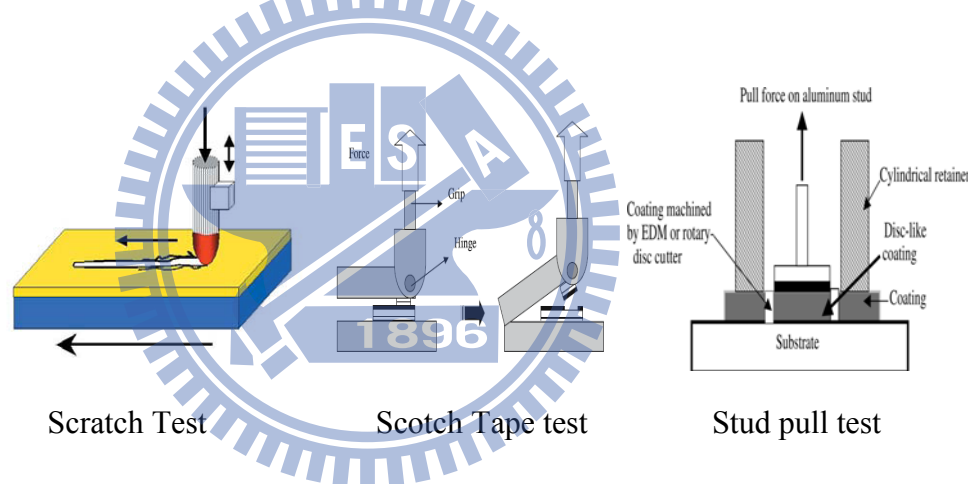


Figure 2. 9. The common techniques for measuring the interfacial strength

2.3 Plasma Surface Modification to Improve the Reliability of Flexible Devices.

The surface properties of materials play important roles in the interfacial interaction phenomena for various applications such as microelectronics, industrial coating, and space technologies. Surface modification can be achieved by a wet, dry or radiation treatment. Among these methods, reactive ion etching is a plasma-based dry etching technique characterized by a combination of physical sputtering with the

chemical activity of reactive species. Recently, plasma treatment has received a great attention for applications of modifying polymer surface and interface. It is believed that the surface functional properties of polymer materials, which can be tailored via chemical reactions (oxygen, fluorine, nitrogen, etc.) with polymer surface [8], are essential for controlling the surface properties and possibly interfacial adhesion as well.

Oxygen plasma has often been employed to improve wetting properties of polymer surface. This has been proposed to result from the formation of various polar groups such as hydroxyl (-OH), carbonyl (-C=O) and ester (-COOR) groups [32]. Metals were observed to interact with these groups on the plasma modified surface. For example, the formation of metal-oxygen-polymer complexes formed on oxygen plasma treated polymer surfaces correlates with adhesion of metal film in Cu/polyimide system [33].

The assignments of peaks and the relative peak area (in %), with respect to the total C 1s integrated area, for each component of these samples are listed in Table 2.2 [34]. In Table 2.2, the relative peak area of C-N bonding remains almost unchanged in the three systems. However, the relative peak area of C-C/C-H, C-O, C=O, and C-F bondings revealed incoherent changes after different plasma treatment. The results of pull tests are shown in Table 2.3 together with surface roughness and chemical

state information in copper/polyimide sample. The improved adhesion was attributed to C-O bonding and surface roughness [35].

Table 2. 2. XPS binding energies and relative peak areas of deconvoluted C 1s spectra obtained from 6FDA-BisAAF fluorinated polyimide before and after different plasma treatment.

Binding energy (eV)[relative peak area (%)]					
C 1s					
Assignment	C-C, C-H	C-N	C-O	C=O	C-F
untreated	285/(53.5)	286.2/(20.9)	-	288.6/(11.1)	292.9/(14.5)
O ₂ plasma	285/(34.2)	286.1/(21.4)	287.4/(17.5)	288.8/(13.6)	292.9/(13.2)
N ₂ plasma	285/(49.3)	286.1/(20.2)	287.3/(5.93)	288.8/(12.6)	292.9/(12.0)

Table 2. 3. Values of the pull strength, surface roughness, and increased chemical states in samples.

	Oxygen plasma etching for 3 min	Dipped into water after oxygen plasma etching
Pull strength (MPa)	30.4	14.7
Roughness Ra (nm)	8	29
Increased chemical component	C-O	C-OH

2.4 Transparent Conductors

The transparent conductors used most often are transparent conducting oxides (TCOs). Transparent conducting oxides are a class of materials that transmit visible radiation and conduct electricity. They find application as the transparent electrodes in numerous applications such as photovoltaics, flat panel displays, heat reflective coatings on energy-efficient windows, and electrochromics such as smart mirrors [36].

The important TCO semiconductors are impurity-doped ZnO, In₂O₃ and SnO₂ as well as multicomponent oxides consisting of combinations of ZnO, In₂O₃, and SnO₂, including some ternary compounds existing in their systems [37]. Tin-doped indium oxide (In₂O₃) is the most common transparent conducting material due to its excellent properties such as high transmittance (90%), a low resistivity in the order of 10⁻⁴ Ω-cm, good thermal and mechanical properties. However, ITO is very expensive. The price of ITO was \$72/kg before 1960 when mostly was used in solder. It was increased to US\$946/kg by 2005, and temporarily reduced to US\$685/kg in 2008. In addition, ITO is toxic, which prompts the development of other, non-toxic TCOs as the alternative [38]. The list of TCOs is shown in Table 2.4. Aluminum-doped ZnO (AZO) is one of the best alternatives in comparison to ITO due to its low resistivity, high transmission, inexpensive and non-toxic characteristics. The comparison of key

attributes and fundamental properties between AZO and ITO thin-film transparent electrodes are summarized in Table 2.5 [37,39].

Table 2. 4. TCO materials for thin-film transparent electrodes

Material	Dopant or compound
SnO ₂	Sb, F, As, Nb, Ta
In ₂ O ₃	Sn, Ge, Mo, F, Ti, Zr, Hf, Nb, Ta, W, Te
ZnO	Al, Ga, B, In, Y, Sc, F, V, Si, Ge, Ti, Zr, Hf
CdO	In, Sn
ZnO–SnO ₂	Zn ₂ SnO ₄ , ZnSnO ₃
ZnO–In ₂ O ₃	Zn ₂ In ₂ O ₅ , Zn ₃ In ₂ O ₆
In ₂ O ₃ –SnO ₂	In ₄ Sn ₃ O ₁₂
CdO–SnO ₂	Cd ₂ SnO ₄ , CdSnO ₃
CdO–In ₂ O ₃	CdIn ₂ O ₄
MgIn ₂ O ₄	
GaInO ₃ , (Ga, In) ₂ O ₃	Sn, Ge
CdSb ₂ O ₆	Y
ZnO–In ₂ O ₃ –SnO ₂	Zn ₂ In ₂ O ₅ –In ₄ Sn ₃ O ₁₂
CdO–In ₂ O ₃ –SnO ₂	CdIn ₂ O ₄ –Cd ₂ SnO ₄
ZnO–CdO–In ₂ O ₃ –SnO ₂	

Table 2. 5. Comparison of thin-film transparent electrode properties between AZO and ITO films

	Doped ZnO	ITO
Low resistivity (Ω cm)	10^{-5}	10^{-5}
Practical resistivity (Ω cm)	$2-3 \times 10^{-4}$	1×10^{-4}
E_g (eV)	3.3	3.7
Index of refraction	2	2
Work function	4.6	4.8–5.0
Cost	Inexpensive	Very expensive
	Stability	
Acid solution	<Good (stable)	
Alkali solution	<Good (stable)	
Oxidizing atmosphere at high temperature (or oxygen plasma)	<Good (stable)	
Reducing atmosphere at high temperature (or hydrogen plasma)	Good (stable)>	

2.5 Effect of Oxygen Plasma Treatment on the Electrical Properties

Electrical properties of CTO materials can be affected by crystal structure, grain size, impurity, roughness of surface, and strain. The crystallinity and grain size can be measure by X-ray diffraction (XRD). Figure 2.10 shows the XRD patterns of the AZO layer (2 wt.% Al-doped ZnO) deposited on the polyethersulfon (PES), poly ethylene terephthalate (PET), and fused quartz (FQ) substrates. There is a very symmetrical (0002) peak (near 34.4°) in the ZnO layer [40]. The grain size as measured by the Scherrer method is given by [41]:

$$D = \frac{0.9\lambda}{\beta \cos \theta} \quad (2.2)$$

where D is the grain size, θ is the Bragg angle, λ is the wavelength of the X-ray, and β is the full-width-half-max of the peak.

The electrical properties of material can affect by impurities, crystal structure, strain, surface roughness, grain size and strain. The plasma treatment modified polymer surface increase crystallinity and grain side due to increase adhesion force [42]. However it also increase interface roughness of materials after deposition.

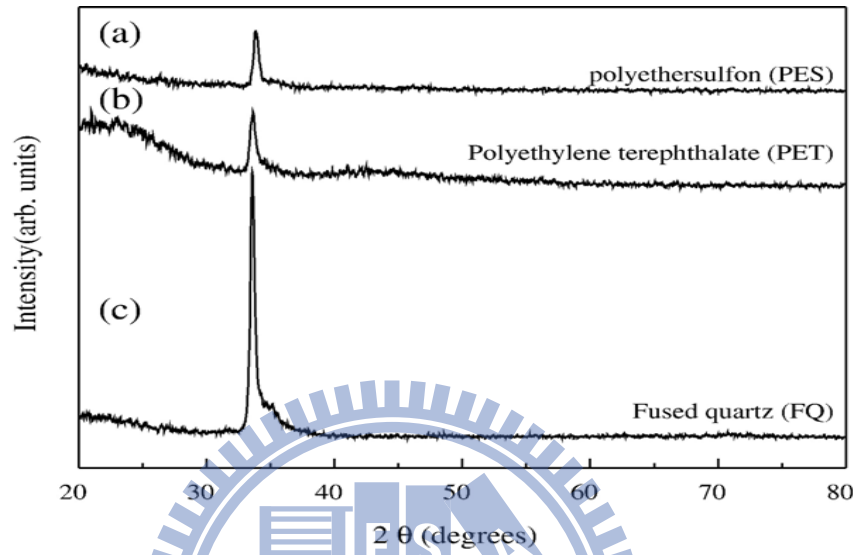


Figure 2. 10. XRD patterns of AZO thin films deposited on (a) PES (b) PET and (c) FQ substrates.

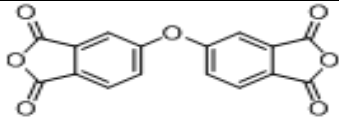
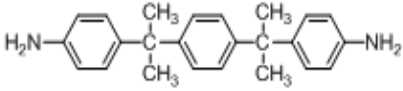
Chapter 3. Experimental Procedures

3.1 Sample Preparation

3.1.1 Synthesis of ODPA-BADB polyimide

ODPA-BADB polyimide was synthesized using two monomers 4,4-oxydiphthalic anhydride (ODPA) and bis(4-aminophenyl)-1,4-diisopropylbenzene (BADB) [43]. N,N-dimethyl-acetamide (DMAC) was a solvent for both ODPA and BADB monomers. The chemical structures and molecular weights of monomers and solvent were listed in Table 3.1. Prior to the use of ODPA, it was re-crystallized in the acetic anhydride. During synthesis, BADB was added in the DMAC and stirred at the room temperature until BADB was completely dissolved. Then, ODPA was added into the solution and stirred for 48 hours at room temperature. ODPA-BADB polyimide film was prepared by spin-coating on the glass substrate at 3000 rpm and heated in an oven from room temperature to 270 °C. Figure 3.1 shows the synthesis reaction of ODPA-BADB polyimide. ODPA-BADB polyimide film with a thickness of 60 μm possesses a high glass transition temperature ($T_g = 252$ °C) and high transmission rate (90%) in the visible light [43].

Table 3. 1. Chemical structures and molecular weights of monomers and solvent.

Chemical	Structure	Molecular weight
ODPA (C ₁₆ H ₆ O ₇)		310.2
BADB (C ₂₄ H ₃₄ N ₂)		344.5
DMAC (C ₄ H ₉ NO)	CH ₃ CON(CH ₃) ₂	87.12

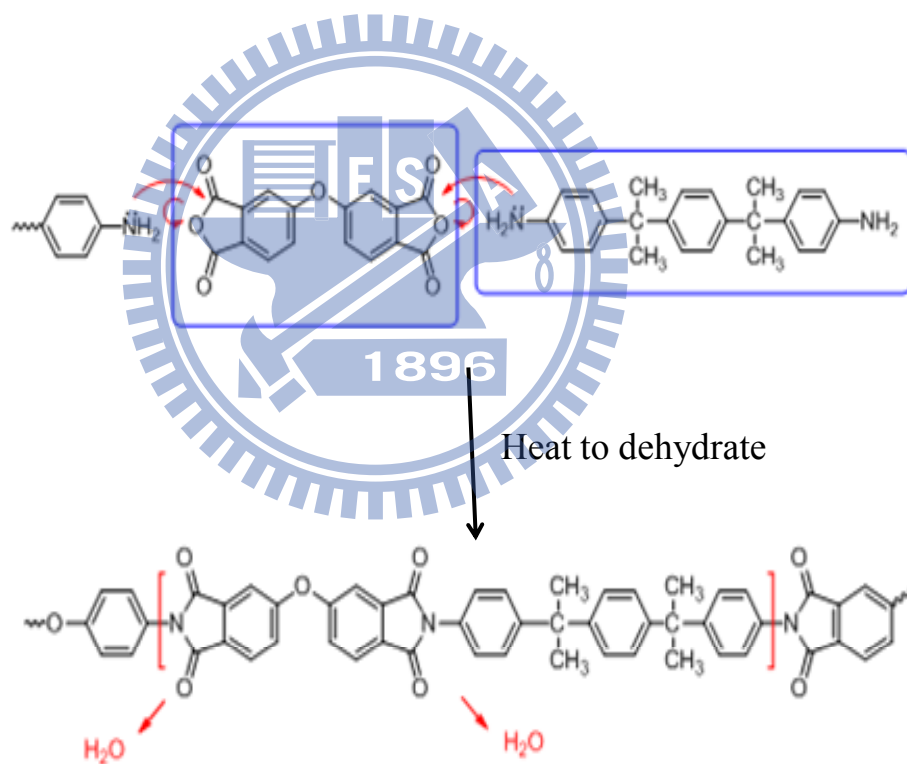


Figure 3. 1. Synthesis reaction of ODPA-BADB polyimide

3.1.2 Surface Modification of Polyimide by Oxygen Plasma

Low-pressure oxygen plasma used for PI surface modification was produced by reactive ionic etching (RIE). Prior to plasma treatment, the samples were heated up to 100 °C in order to remove the absorbed water, then the sample surface was cleaned by argon gas. The conditions of plasma treatment PI are shown in Figure 3.2, where the gas flow rate and pressure were kept the same. In this thesis, the effects of plasma power and treatment time on the surface and interfacial adhesion were investigated.

Table 3. 2. Plasma treatment conditions of ODPa-BADB polyimide film

Gas	Flow rate (sccm)	Pressure (mtorr)	Power (W)	Time (min)
Oxygen	20	50	100	5
	20	50	50	1
	20	50	50	3
	20	50	50	5
	20	50	50	7

3.1.3 Deposition of Aluminum-Doped Zinc Oxide (AZO) Film

200 nm thick Al-doped (2% wt) ZnO (AZO) films were deposited onto 2.5 μm thick polyimide films/silicon substrate by sputtering ceramic AZO target in a physical vapor deposition (PVD) system at room temperature. The deposition parameters affecting the characteristics of the AZO film included: (1) temperature of the

deposition chamber, (2) total gas flow, and (3) power. For this study, the deposition parameters for AZO film on PI are summarized in Table 3.3. The growth rate and thickness will be examined by SEM in Chapter 4.

Table 3.3. Deposition parameters for AZO film on PI

Deposition parameters	Conditions
RF power	70W
Working pressure	7.5×10^{-3} mtorr
Substrate temperature	RT
Argon flow rate	30 sccm
Time	55mins

3.1.4 Measurement Procedure and Data Analysis for Four Point Bending Adhesion Test

The sample preparation steps for four-point bending test are schematically illustrated in Fig. 3.2. The epoxy resin was deposited onto the silicon wafer by using a 2-step spin-coating: step 1 at 3000 rpm for 20 seconds and step 2 at 5000 rpm for 40 seconds. Thick Si wafers and small clamps were used to distribute the applied force by C-clamp as shown in Figure 3.3. The sandwich sample was then heated in an oven at 150° for 1 hour to make the sample and blank wafer inseparable. After the sandwich sample was cooled down to room temperature in an oven, it was cut into the size of $7\text{cm} \times 0.5\text{cm}$ to fit for four-point bending test. A $400\sim 500\ \mu\text{m}$ pre-notch was created in the middle by using a diamond saw. The stacking structure of sandwich sample and schematic drawing of four point bending test sample are illustrated in Figure 3.4.

Figure 3.5 shows the typical load-displacement graph of four-point bending test. The weakest interface is peeled off through pre-notch propagation. Adhesion energy (G_c) is readily calculated by observing the plateau in the load-displacement curve [44,45].

The corresponding G_c is given by:

$$G_c = \frac{21(1-\nu^2)P_c^2 L^2}{16EB^2 h^3} \quad (3.1)$$

Where: P_c : Critical load

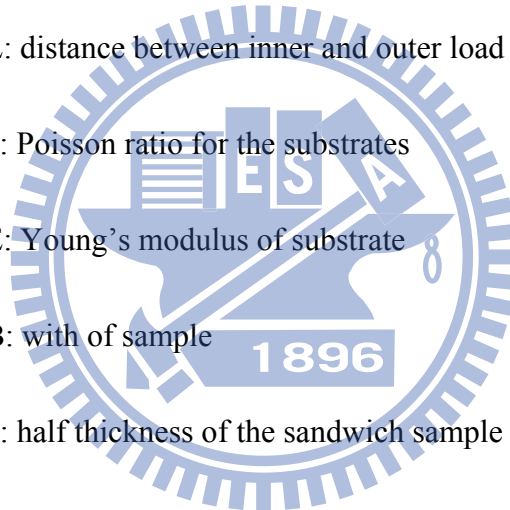
L: distance between inner and outer load points

ν : Poisson ratio for the substrates

E: Young's modulus of substrate

B: width of sample

h: half thickness of the sandwich sample



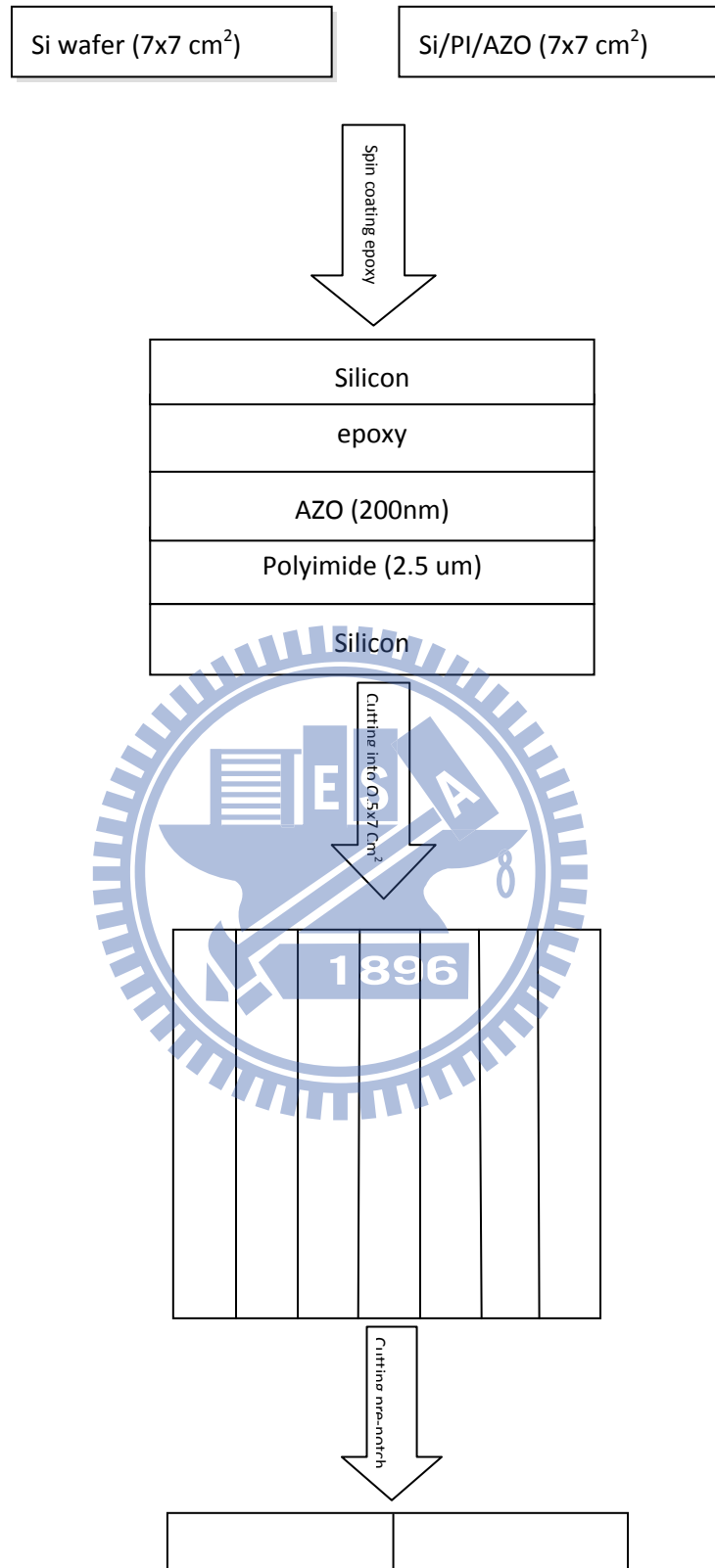


Figure 3.3. Sample preparation steps for four point bending test



Figure 3. 4. C-clamp and small clamps for fixing four point bending sample

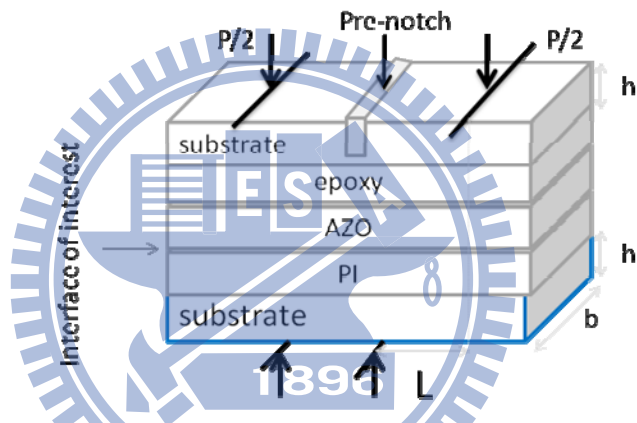


Figure 3. 5. The stacking structure of sandwich sample and schematic drawing of four point bending test sample

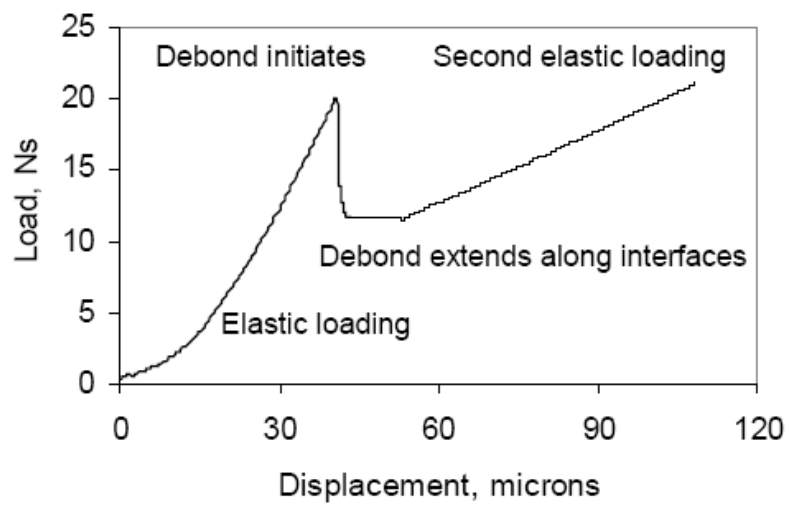


Figure 3.6. A typical load and displacement curve for four point bending test

3.2 Experimental Method and Procedures

Figure 3.6 summarizes the flow-chart of experimental procedures and characterization techniques in this thesis. First, the polyimide surface was treated by oxygen plasma using a reactive ionic etcher (RIE, model: AST Cire-200). The surfaces properties such as surface chemical states, surface roughness, and surface energies of oxygen plasma modified polyimide films were characterized by using x-ray photoelectron spectroscopy (XPS) (ULVAC-PHI, PHI Quantera SXM2), atomic force microscope (AFM), and contact angle measurement, respectively. The adhesion of ITO/PI interface was measured by a home-built four-point bending system. In addition, the resistivity of AZO film was measured by four-point probe. The crystal structure and grain size were characterized by using X-ray diffraction (Siemens Diffractometer D5000, Cu $K\alpha$, $\lambda=1.5405\text{\AA}$).

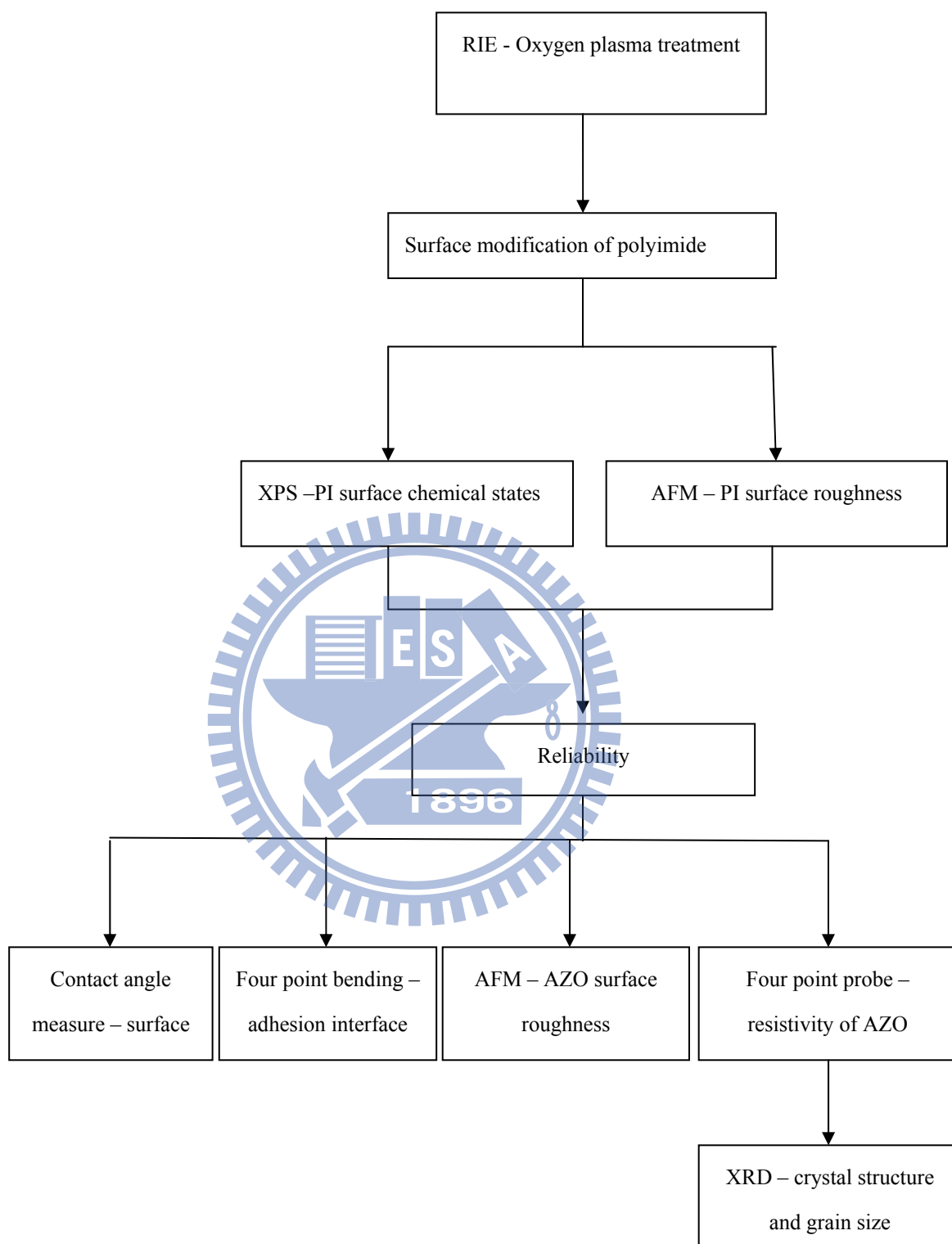


Figure 3. 7. Flow – chart of experimental procedures and characterization

3.3 Introduction of Instruments

3.3.1 Reactive Ionic Etching (RIE)

The principle of reactive ionic etching was shown in Figure 3.7 [46]. The wafer was parallel with the plate reactor. Plasma is initiated at low plasma potential in the system by applying a strong RF electromagnetic field to the wafer plate reactor. RIE is a dry etching technique, which combines the physical sputtering with the chemical activity of reactive type. The different gas source (oxygen, nitrogen, argon ...) is used to react to sample. [47]. An important feature of RIE is its ability to achieve etch directionality [48]. In my research, RIE was used to create oxygen plasma treatment to modify the polyimide surface using different power and treatment time.

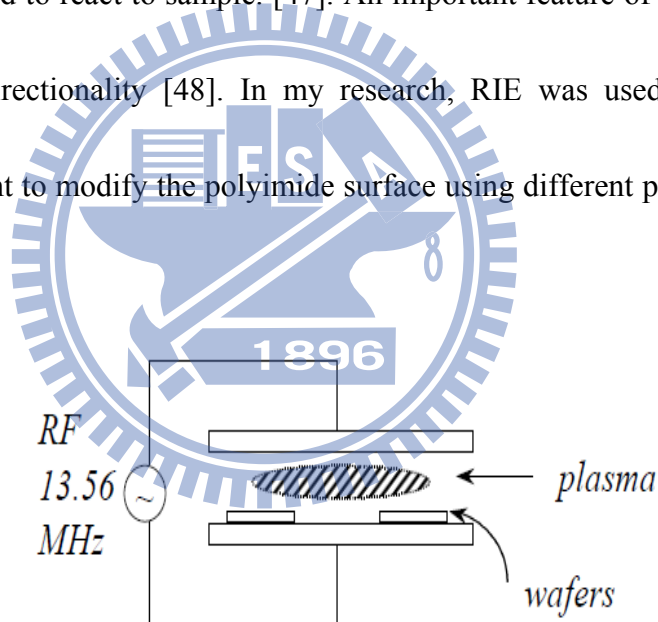


Figure 3. 8. The principle of reactive ionic etching

3.2 X-ray Photoelectron Spectroscopy (XPS)

X-Ray photoelectron spectroscopy (XPS), also known as electron spectroscopy for chemical analysis (ESCA), is an analysis technique used to obtain chemical information about the surfaces of solid materials. Both composition and the chemical

state of surface constituents can be determined by XPS. Insulators and conductors can easily be analyzed in surface areas from a few microns to a few millimeters across. The XPS instrument was illustrated in Figure 3.8 [49]. XPS instruments consist of an x-ray source, an energy analyzer for the photoelectrons, and an electron detector. The analysis and detection of photoelectrons require that the sample be placed in a high-vacuum chamber. Since the photoelectron energy depends on x-ray energy, the excitation source must be monochromatic. The energy of the photoelectrons is analyzed by an electrostatic analyzer, and the photoelectrons are detected by an electron multiplier tube or a multichannel detector such as a microchannel plate. Figure 3.9 [50] shows that the X-ray source can irradiate and remove the e^- from the core level causing the e^- to leave the atom. However, only the electrons in top layer can move outer surface, other ones will be kept by collision with atoms. Thus, the XPS only measure on some nanometer the surface of a sample.

The composition chemical bonding of the polyimide thin films were investigated by using XPS (ULVAC-PHI, PHI Quantera SXM2). The photoelectron emission spectra was obtained using an Al X-ray source (1486.6eV) striking the surface of the sample. The analyzer resolution was fixed at 0.01 eV. Ar^+ ion was used to remove adsorbed surface contaminants for 5 seconds before analysis. The insulating properties of these deposits caused surface charging effects, resulting in electron lines

being shifted to lower kinetic energies. However, the electronic-gun in the XPS could be neutralization and diminished the surface charge effects. The peak positions were calibrated with respect to the position of C 1s carbon contamination peak usually located at about 285 eV.

In XPS the photon is absorbed by an atom in a molecule or solid, leading to ionization and the emission of a core (inner shell) electron. the difference in energy between the ionized and neutral atoms, is generally called the binding energy (BE) of the electron - this then leads to the following commonly quoted equation[51] :

$$KE = h\nu - BE \quad (3.2)$$

where

KE : energy of photoelectron

$h\nu$: photon energy from the X-Ray source

BE: binding energy

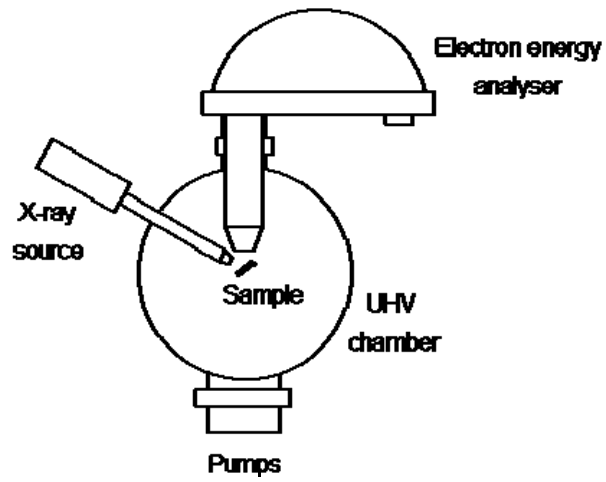


Figure 3.8. The XPS instrument

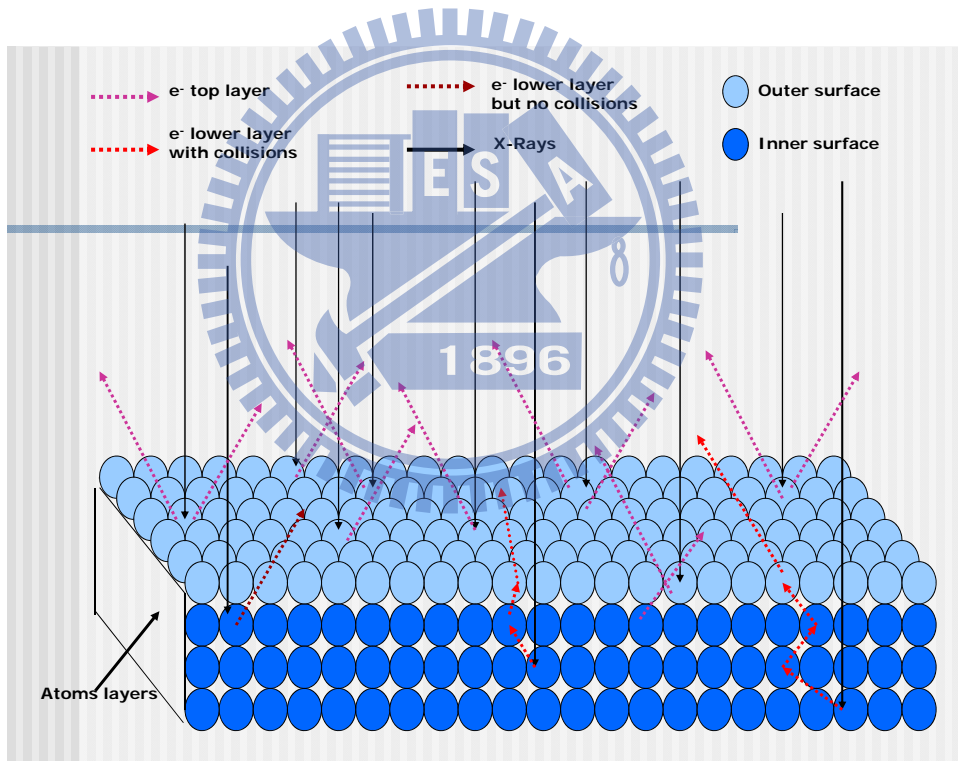


Figure 3.9. X-rays and electrons on the surface during XPS measurement

3.3.3 Curve Fitting XPS Data

The analysis of XPS spectra has been carried out using the XPS peak fitting program for WIN95/98 XPSPEAK Version 4.1 that have been created by Raymond W. M. Kwok [52]. The surface chemical states analysis of BAPP-ODPA polyimide had been illustrated by Figure 3.10. This program uses the following asymmetric Gaussian-Lorentzian sum function. However, The Gaussian distribution was used for the calculation of each specific peak and the value of Gaussian distribution had been fixed at zero. Another parameter needed to fix in the peak fitting software was the full width at half maximum (FWHM). The main algorithm used in this software is Newton's method for optimization, while Shirley and Linear background were employed [52]. Only the peak position was assigned by an operator, and the same values for all other parameters were used for every XPS chart to investigate the consistent intensity of the functional groups [53].

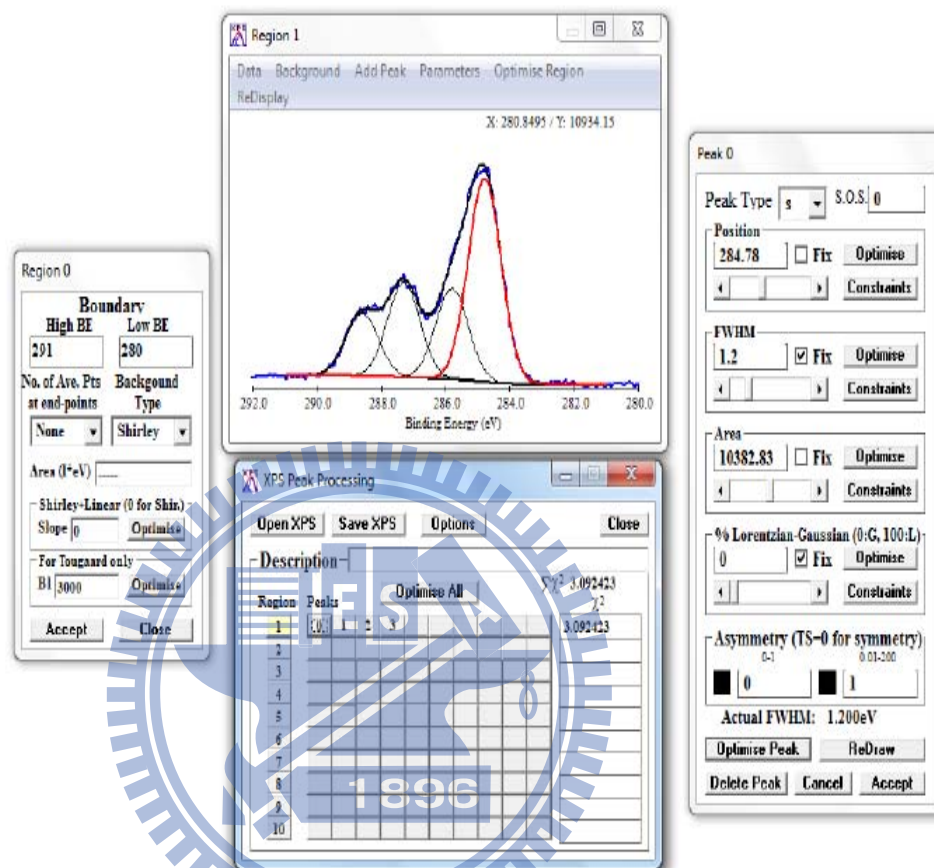


Figure 3. 9. The XPS peak fitting program

3.3.4 Atomic Force Microscope (AFM)

AFM consists of a scanning sharp tip at the end of a flexible cantilever across a sample surface while maintaining a small, constant force [54]. The tips typically have an end radius of 2 nm to 20 nm, depending on a tip type. The scanning motion is conducted by a piezoelectric tube scanner which scans the tip in a raster pattern with respect to the sample (or scans to the sample with respect to the tip). The tip-sample interaction is monitored by reflecting a laser off the back of the cantilever into a split photodiode detector. By detecting the difference in the photodetector output voltages, changes in the cantilever deflection or oscillation amplitude are determined. A schematic diagram of this mechanism is depicted in Fig. 3.11[55].

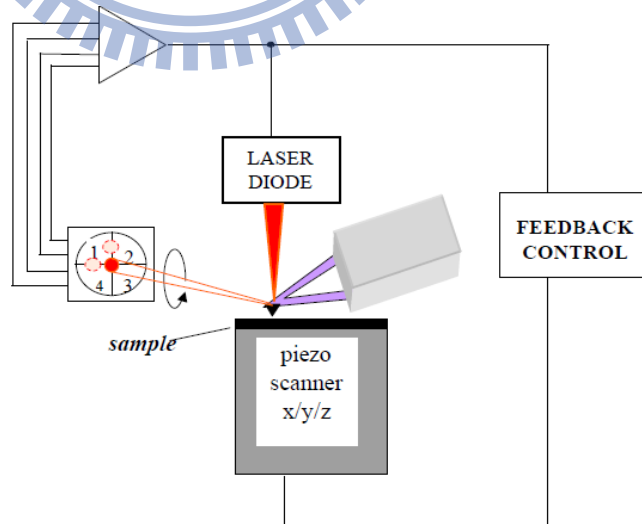
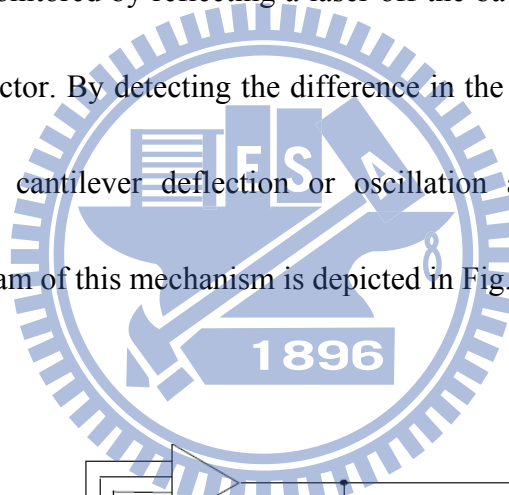


Figure 3. 10. AFM – schematic principle

The two most commonly used modes of operation are contact mode AFM and tapping mode AFM, which are conducted in air or liquid environments. Contact mode AFM consists of scanning the probe across a sample surface while monitoring the change in cantilever deflection with the split photodiode detector. A feedback loop maintains a constant cantilever deflection by vertically moving the scanner to maintain a constant photodetector difference signal. The distance the scanner moves vertically at each x, y data point is stored by the computer to form the topographic image of the sample surface. This feedback loop maintains a constant force during imaging, which typically ranges between 0.1 to 100 nN. [56].

Tapping mode AFM consists of oscillating the cantilever at its resonance frequency (typically ~300 kHz) and lightly “tapping” on the surface during scanning. The laser deflection method is used to detect the root-mean-square (RMS) amplitude of cantilever oscillation. A feedback loop maintains a constant oscillation amplitude by moving the scanner vertically at every x, y data point. Recording this movement forms the topographical image. [57] The advantage of Tapping Mode over contact mode is that it eliminates the lateral, shear forces present in contact mode, enabling tapping mode to image soft, fragile, and adhesive surfaces without damaging them, which can be a drawback of contact mode AFM.

3.3.5 Contact Angle Measurement

Figure 3.12 shows the schematic diagram of a contact angle measurement system [58]. Contact angle is measured by a contact angle goniometer using an optical subsystem to capture the profile of a pure liquid on a solid substrate. The angle formed between the liquid/solid interface and the liquid/vapor interface is the contact angle. Older systems used a microscope optical system with a back light. Current-generation systems employ high resolution cameras and software to capture and analyze the contact angle.

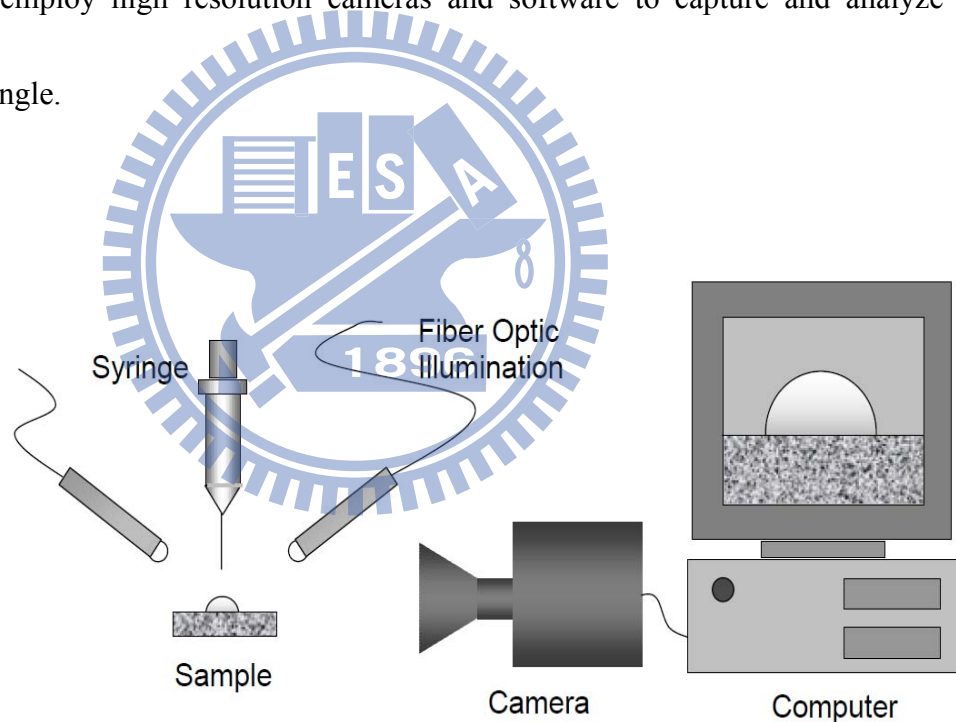


Figure 3. 11. Schematic diagram of a contact angle measurement system

Contact angles on PI surfaces were measured with pure water. The surface energies were calculated using Young's Equation [59] :

$$\sigma_s = \sigma_{sl} + \sigma_l \cos\theta \quad (3.3)$$

where θ : contact angle

σ_s : surface energy of solid

σ_l : surface tension of the liquid

σ_{sl} : wetting tension.

The surface tension of pure water is 72 dyne/cm.

Thus, the surface energy of polyimide can be calculated [60] after contact angle and wetting tension are obtained from this measurement.

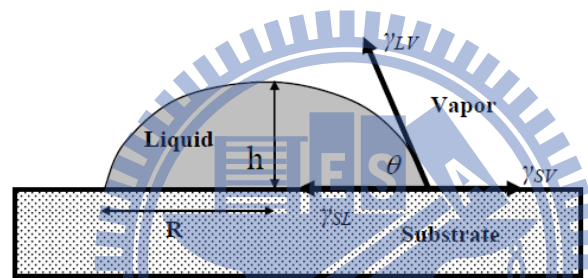


Figure 3. 12. Contact angle θ of liquid drop on solid [61] .

3.3.6 Scanning Electron Microscopy (SEM)

The scanning electron microscope (SEM) is a type of electron microscope that use the high energy beam to image the sample surface. The electron react with atoms in sample surface and products the information of surface sample topography [62]

In a typical SEM shown in Figure 3.14, [63] an electron beam is thermionically emitted from an electron gun fitted with a tungsten filament cathode. The electron beam, which typically has an energy ranging from 0.5 keV to 40 keV, is focused by one or two condenser lenses to a spot about 0.4 nm to 5 nm in diameter.

The beam passes through pairs of scanning coils or pairs of deflector plates in the electron column, typically in the final lens, which deflect the beam in the x and y axes so that it scans in a raster fashion over a rectangular area of the sample surface.

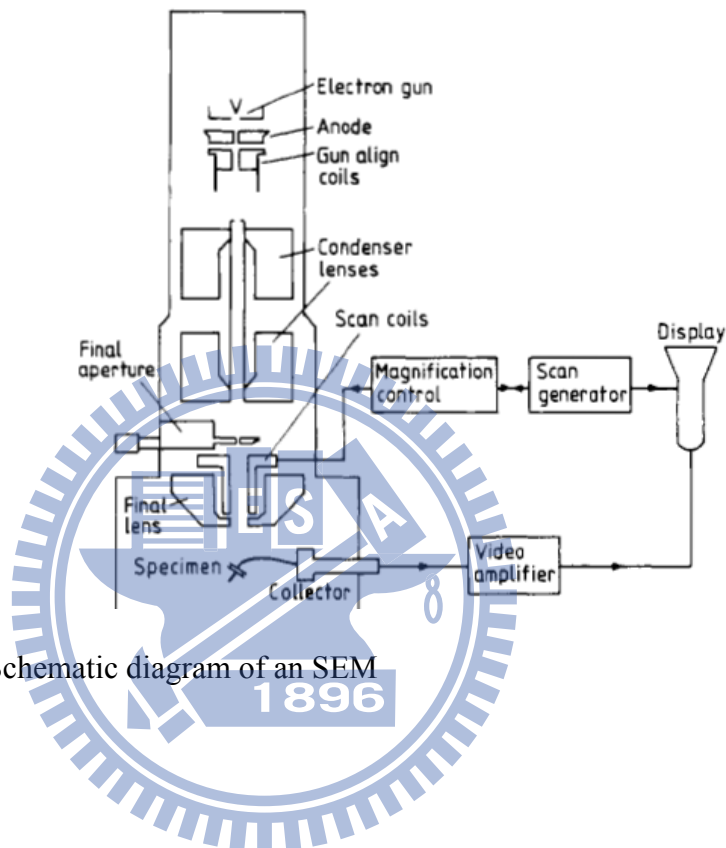


Figure 3. 13. Schematic diagram of an SEM

3.3.7 Physical-Vapor Deposition

Physical vapor deposition (PVD) is a method of depositing thin films by sputtering material from a target, which then deposits onto a substrate. Resputtering is re-emission of the deposited material during the deposition process by ion or atom bombardment. The simple schematics of the sputtering process is shown in Figure 3.15 [64]. Al-doped ZnO (AZO) thin films were deposited on PI substrate using a

PVD system (Psur 100 HC Advantage System Technology), which uses high vacuum RF sputtering with argon as the sputtering gas.

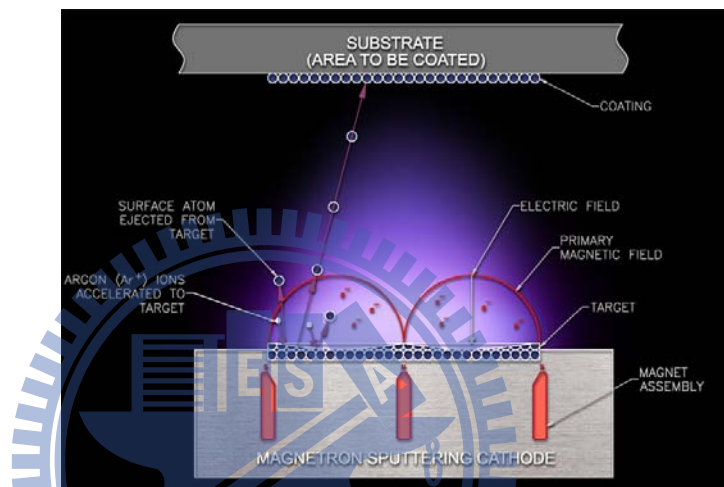


Figure 3. 14. PVD sputtering system

3.3.8 Four Point Bending System

Figure 3.16 shows the home-built four point bending system [65]. The sandwich sample of four point bending test were put between the two inner and tow outer in sample holder. The samples were pulled by the linear motorized actuator. The displacement of load point was controlled by motion control card at the range of velocity from 0.1 $\mu\text{m/s}$ to 200 $\mu\text{m/s}$ which have sensitivity in 0.1 $\mu\text{m/s}$. The load cell with the capacities of 20N or 100N is used to measure the output of

load. Motion – control box contact with stepper to control the displacement of load point. Digital multimeter, which is connected to the detector of load cell, measures and records the real voltage of the detector. The amplifier was used to amplify the voltage. The test system is operated using Labview software, and the displacement and output of load are recorded. The critical load is measured to calculate the critical energy release rate G_c under a steady growth state of crack at an interface.

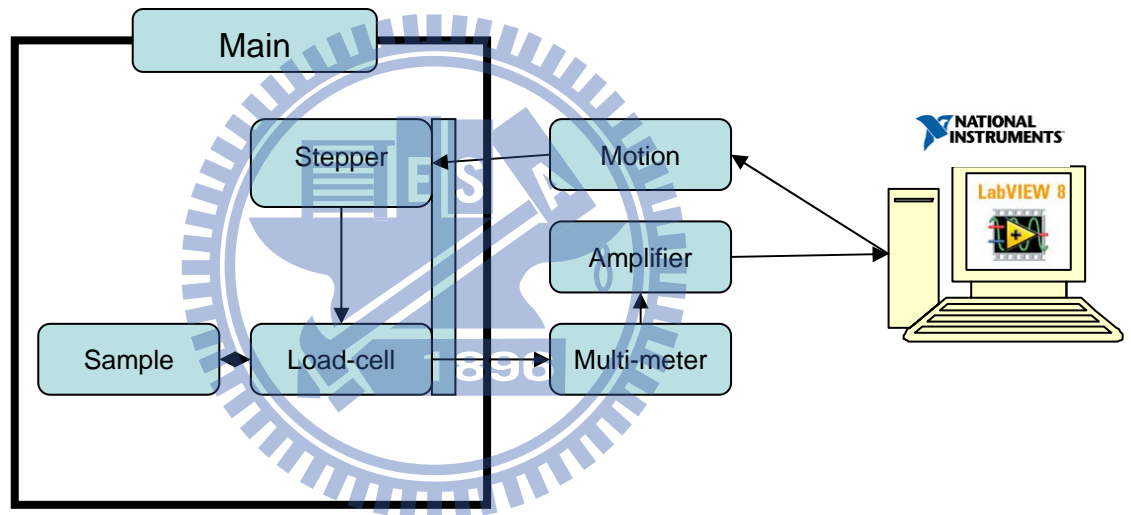


Figure 3. 15. Schematic diagram of four point bending system

3.3.9 Four Point Probe System

A four point probe is a simple apparatus for measuring the resistivity of samples. By passing a current through two outer probes and measuring the voltage

through the inner probes allows the measurement of the substrate resistivity. The four point probe measurement technique was shown in Figure 3.17 [66]. Probe force, probe travel, tip radius and probe material must be selected with consideration for the resistivity, hardness, and thickness of the layer to be measured. We consider a four point probe on a rectangular sample. In addition, the probe is arranged symmetrically with point spacing. The four point probe unit has a $5\ \mu\text{m}$ pitch. The cantilever is $25\ \mu\text{m}$ long and has a thickness of $3\ \mu\text{m}$ and width $5\ \mu\text{m}$. The unit is connected to the electronic circuitry by suitable feed-through. Touch-down is realized by slowly moving downward with the MM3A while monitoring a DC voltage offset, which drops upon touch-down.

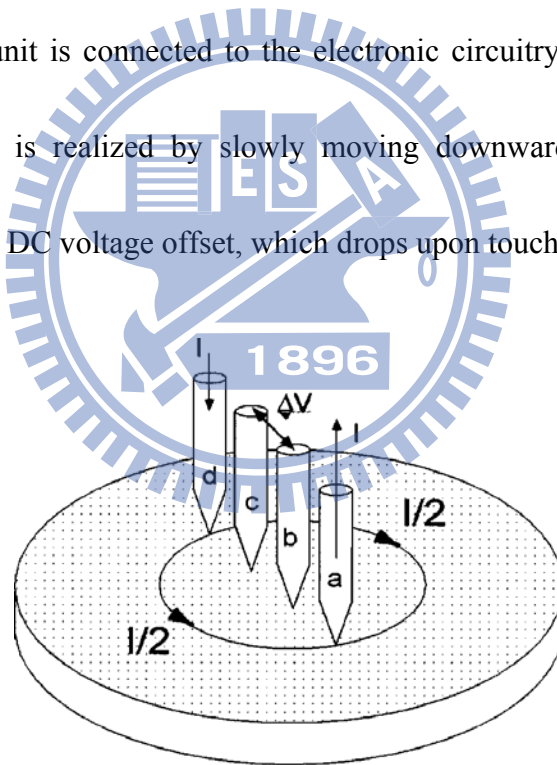


Figure 3. 16. Arrangement of a four-point probe on a rectangular sample

3.3.10 X-ray Diffraction (XRD)

X-ray diffraction (XRD) is a non-destructive tool for analyzing material properties such as crystallinity, the phase identification, and orientation. In addition, grain size and strain can also be easily analyzed with this technique.

XRD was utilized to analyze the crystallinity in this study. The samples were scanned by Siemens Diffractometer D5000 with Cu K_{α} ($\lambda=1.5405\text{\AA}$) source.

During scanning period, X-ray beam of wavelength λ was irradiated to the sample at an angle θ , and the diffracted intensity at an angle 2θ was recorded by a detector

as illustrated in Figure 3.18.

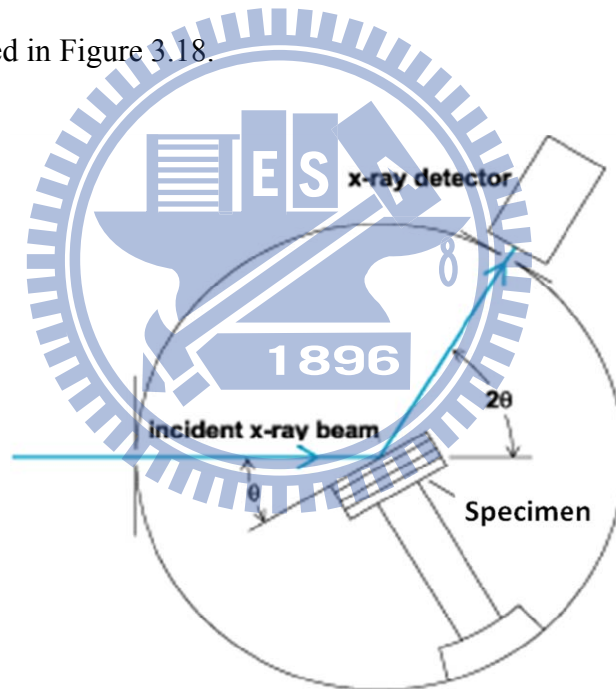


Figure 3. 17. Definition of the angle of incidence and diffraction in an XRD experiment

Chapter 4 Results and Discussion

4.1 XPS Analysis of Surface Chemical States of ODP A-BADB Polyimide

The repeating unit of ODP A-BADB polyimide was illustrated in figure 4.1, It contained eight types of carbon atoms and two types of oxygen. C1s spectrum includes eight main components. However, we limited fitting of C1s signal to three main carbon components, which can be broken in the plasma treatment process [67]. The binding energy of the main components fitting in C1s and O1s signal was listed in table 1. [68]

The binding energy was corrected by comparing real Au peak in experiment with ideal peak. The shift of binding energy was found 1.7 eV, this value was used to correct data in the fitting peak process. The binding energies and composition quantification of ODP A-BADB polyimide before and after oxygen plasma treatment was characterized from table 4.2 to table 4.9 correspond with XPS C1s and O1s spectra were illustrated in Figure 4.2 through Figure 4.9. The component ratios were determined from percent area of each component in the XPS spectra.

Table 4.2 showed the surface component ratio of untreated ODP A-BADB polyimide, it includes three components, namely C-C (284.8eV), C-O-C (285.8eV) and C=O (288.6 eV) due to the component ratios 83.58 %, 10.08 % and 6.34 %. Table 4.3 listed the PI surface components after using oxygen plasma treatment at 50W RF power for 1 minute. The result showed the component ratio of C-C bonding

decrease from 85.53% to 45.43%, the polar groups as C-O-C and C=O increased from 10.08% to 19.5% and 6.34 to 13.95 %. The new polar group C-OH occurred at a position peak 283.7 eV and increase from 0% to 21.12%. Table 4.4 and table 4.5 summarized the PI surface components modified by oxygen plasma treatment at 50W RF power and 100W RF power for 5 minutes. The components ratio were similar with the result in table 4.3. Therefore we can conclude the polar groups ratio increase after oxygen plasma treatment and independence with condition treatment.

The binding energy of O1s was fixed as 532 eV [69], the untreated PI surface components' ratio was listed in table 4.6 include two components C-O-C and C=O with the components ratio were 41.1% and 58.9%, respectively. After Oxygen plasma treated at 50W RF power for 1 minute, the component ratio of C-O-C and C=O decrease from 41.1% to 20.8% and 58.9 to 36.67%. The new component C-OH occurred and increased from 0% to 42.53 %. The surface chemical states of polyimide treated by oxygen plasma at 50W RF power and 100W RF power for 5 minutes was shown in table 4.8 and 4.9. The component's ratio similar and independent with power treatment and time treatment.

The C1s and O1s spectra and fitted peaks of PI film before and after treatment were shown in Figure 4.2 through Figure 4.9. New contribute correspond with C-OH

bonding was found as C9 in the carbon 1s spectra and O3 in oxygen 1s spectra showed.

The reason of formation new group will be discuss later.

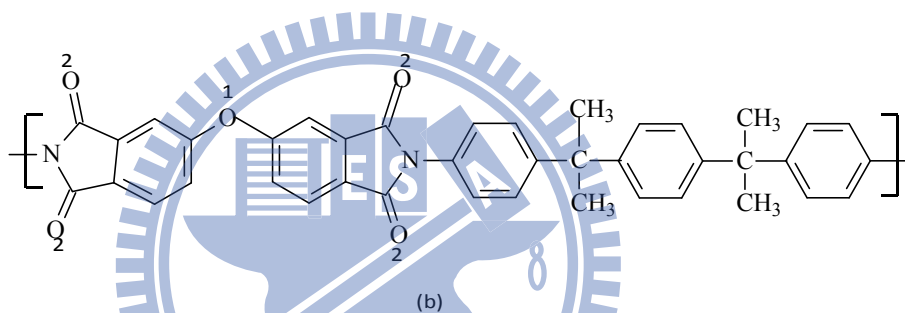
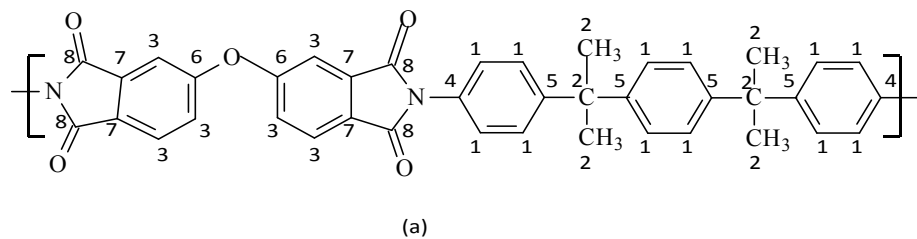


Figure 4. 1. Binding states of the (a) carbon and (b) oxygen atoms in the repeating unit of ODPA-BADB polyimide

Table 4. 1. Main components and their binding energies fitting in C 1s and O 1s

XPS signals of ODPA-BADB polyimide

Signal	Component	Binding energy
--------	-----------	----------------

C1s	C2 (C-C)	284.8
	C6 (C-O-C)	285.8
	C8 (C=O)	288.6
	C9 (C-OH)	287.3
O1s	O1 (C-O-C)	533.3
	O2 (C=O)	532.0
	O3 (C-OH)	532.5

Table 4. 2. Carbon 1s spectrum: binding energies and composition quantification of untreated ODPA-BADB polyimide film.

Component	Peak BE (ev)	Area	%
C-C	284.8	12009.29	83.58
C-O-C	285.8	1448.87	10.08
C=O	288.6	910.98	6.34

Table 4. 3. Carbon 1s spectrum: binding energies and composition quantification of ODPA-BADB polyimide film modified by oxygen plasma at 50W RF Power, time treatment for 1min

Component	Peak BE (ev)	Area	%
C-C	284.8	10473.74	45.43

C-O-C	285.8	4503.04	19.5
C=O	288.6	3216.95	13.95
C-OH	287.3	4861.73	21.12

Table 4.4. Carbon 1s spectrum: binding energies and composition quantification of ODPA-BADB polyimide film modified by oxygen plasma at 50W RF Power, time treatment for 5 min

Component	Peak BE (ev)	Area	%
C-C	284.8	11416.57	46.32
C-O-C	285.8	4467.45	18.13
C=O	288.6	3340.14	13.55
C-OH	287.3	5421.54	22

Table 4. 5. Carbon 1s spectrum: binding energies and composition quantification of ODPA-BADB polyimide film modified by oxygen plasma at 100W RF Power, time treatment for 5min

Component	Peak BE (ev)	Area	%
C-C	284.8	7946.78	46.55
C-O-C	285.8	3216.5	18.84
C=O	288.6	2159.07	12.65
C-OH	287.3	3748.63	21.96



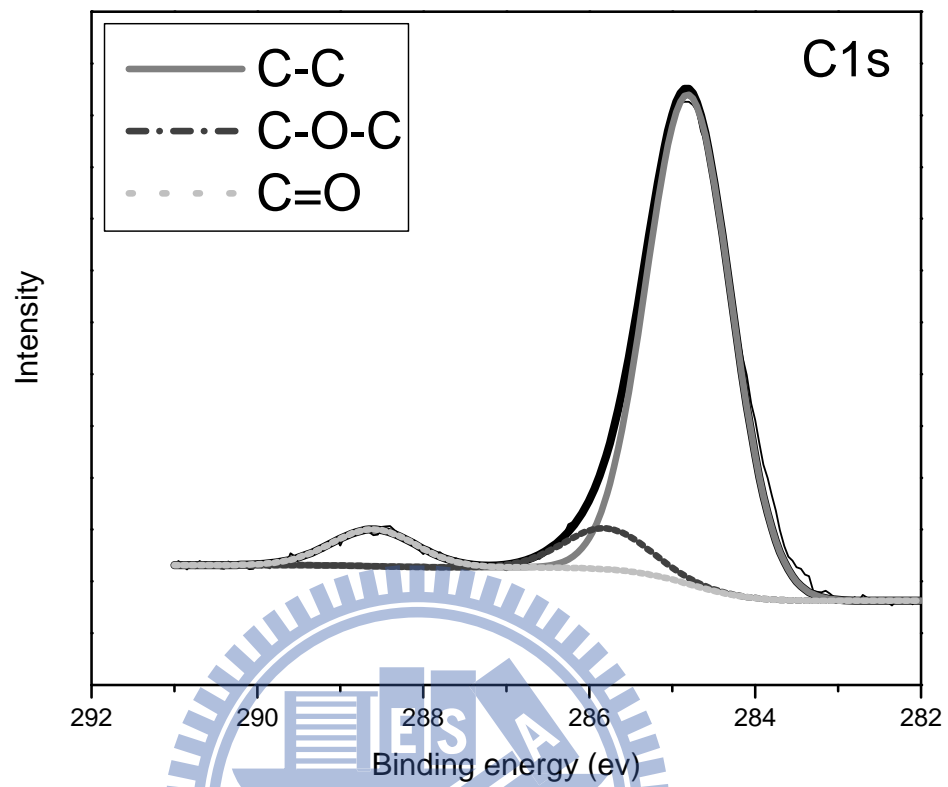


Figure 4. 2. The XPS C 1s spectra of untreated ODPA-BADB polyimide films

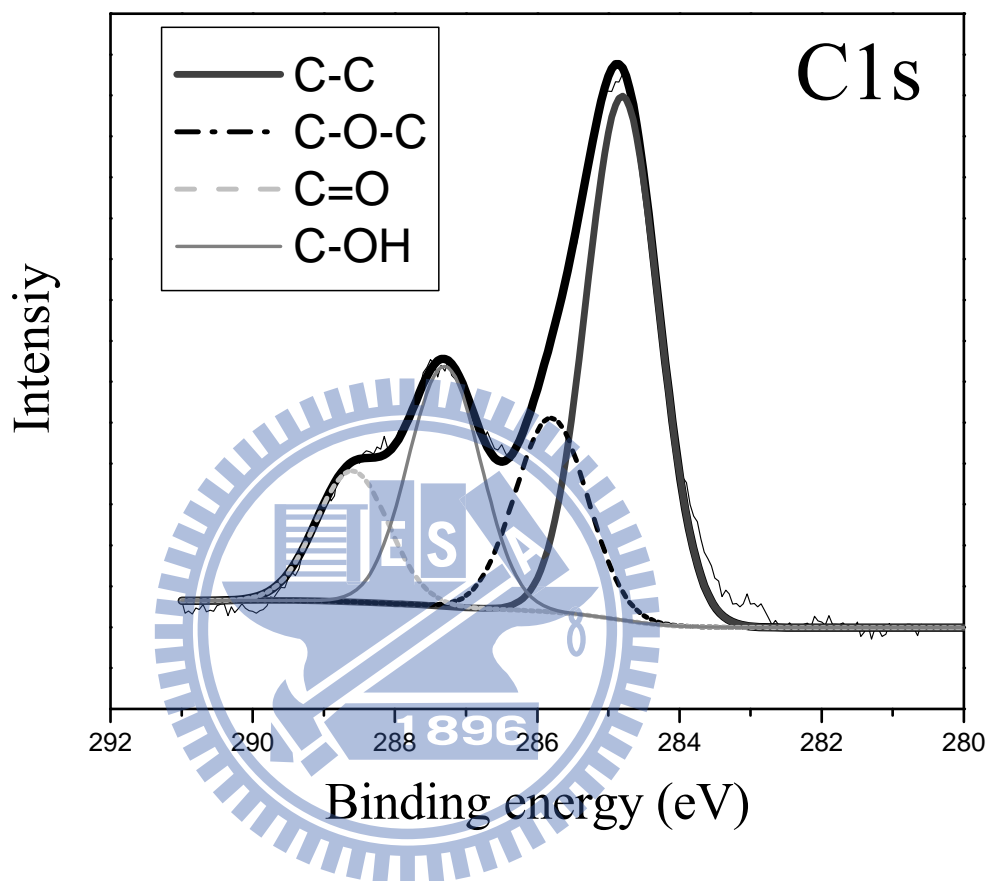


Figure 4. 3. The XPS C 1s spectra of ODPA-BADB polyimide films oxygen plasma treated at 50W RF Power, time treatment for 1min

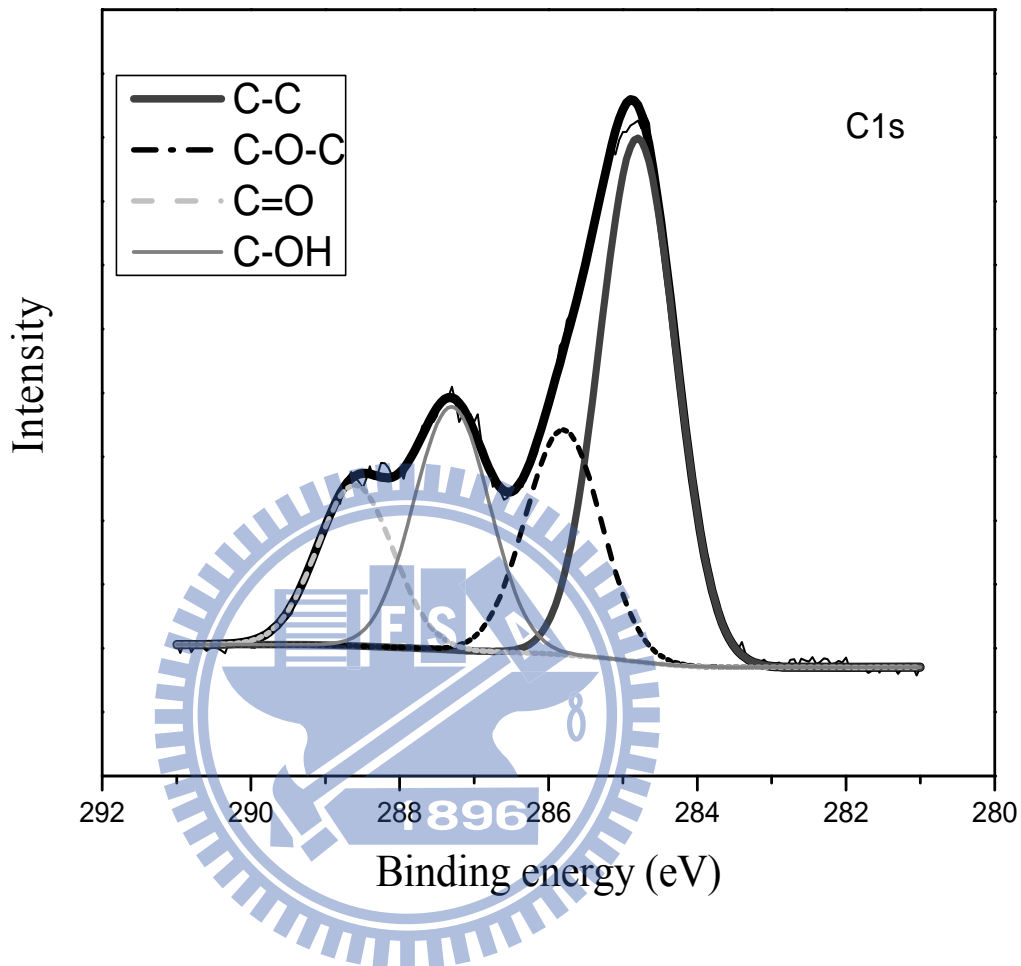


Figure 4. 4. The XPS C 1s spectra of ODPA-BADB polyimide films oxygen plasma treated at 50W RF Power, time treatment for 5 mins

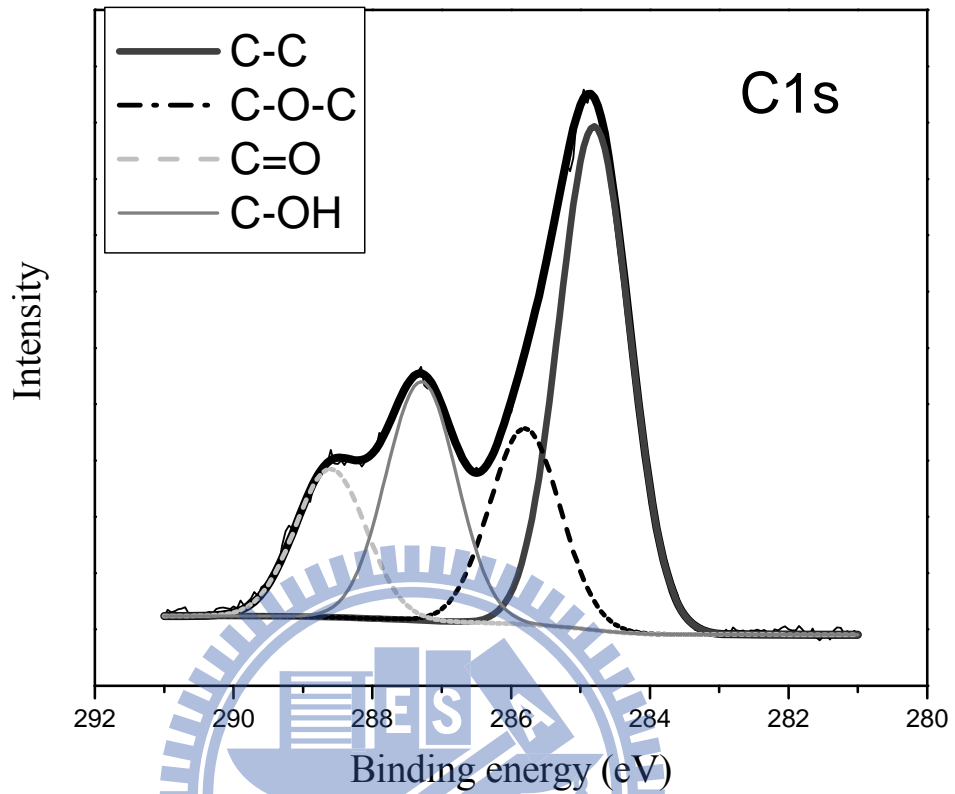


Figure 4. 5. The XPS C 1s spectra of ODPA-BADB polyimide films oxygen plasma treated at 100W RF Power, time treatment for 5 mins

Table 4. 6. Oxygen 1s spectrum: binding energies and composition quantification of untreated ODPA-BADB polyimide film

Component	Peak BE (eV)	Area	%
C-O-C	533.3	4013.76	41.1
C=O	532	5749.93	58.9

Table 4. 7. Oxygen 1s spectrum: binding energies and composition quantification of ODPA-BADB polyimide film modified by oxygen plasma at 50W RF Power, time treatment for 1min

Component	Peak BE (eV)	Area	%
C-O-C	533.3	2894.21	20.8
C=O	532	5099.6	36.67
C-OH	532.5	5912.84	42.53

Table 4. 8. Carbon 1s spectrum: binding energies and composition quantification of ODPA-BADB polyimide film modified by oxygen plasma at 50W RF Power, time treatment for 5 mins

Component	Peak BE (eV)	Area	%
C-O-C	533.3	3216.81	21.45
C=O	532	5365.8	35.8
C-OH	532.5	6402.73	42.75

Table 4.9. Oxygen 1s spectrum: binding energies and composition quantification of ODPA-BADB polyimide film modified by oxygen plasma at 100W RF Power, time treatment for 5 mins

Component	Peak BE (eV)	Area	%
C-O-C	533.3	3471.87	21.9
C=O	532	5613.708	35.4
C-OH	532.5	6781.33	42.7

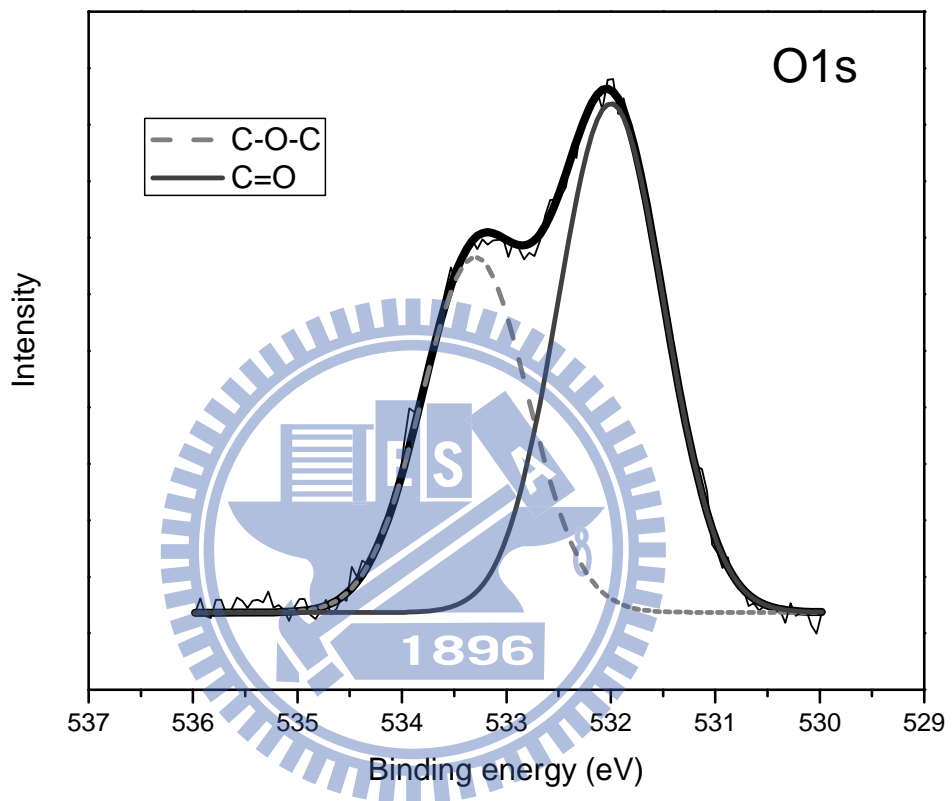


Figure 4. 6. The XPS C 1s spectra of untreated ODPA-BADB polyimide films

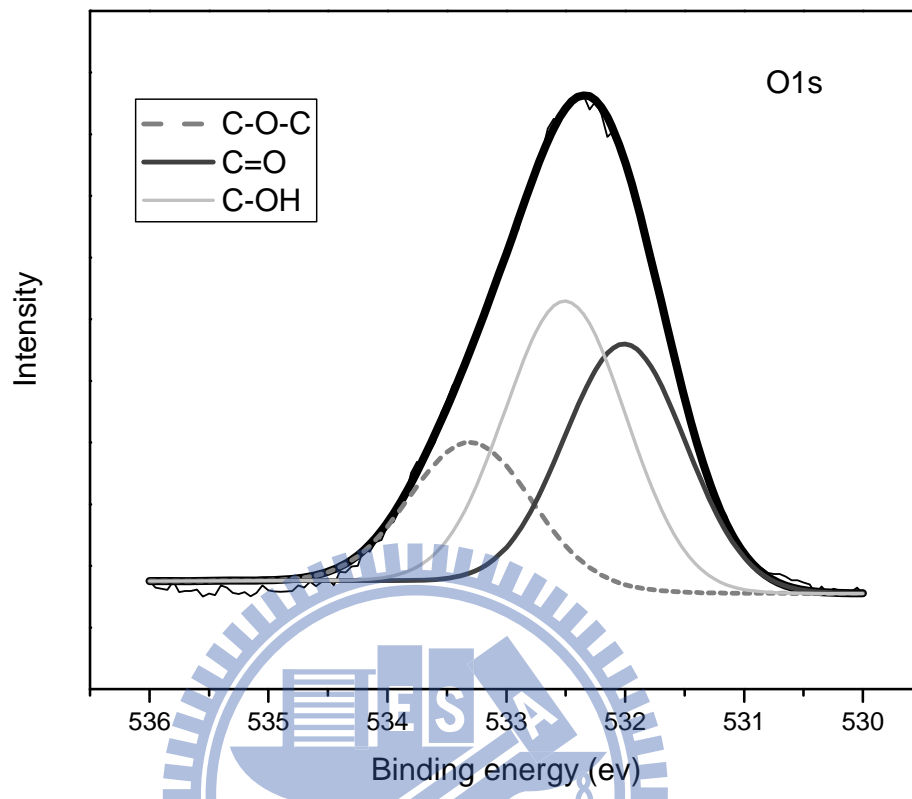


Figure 4. 7. The XPS O1s spectra of ODPA-BADB polyimide films oxygen plasma treated at 50W RF Power, time treatment for 1min

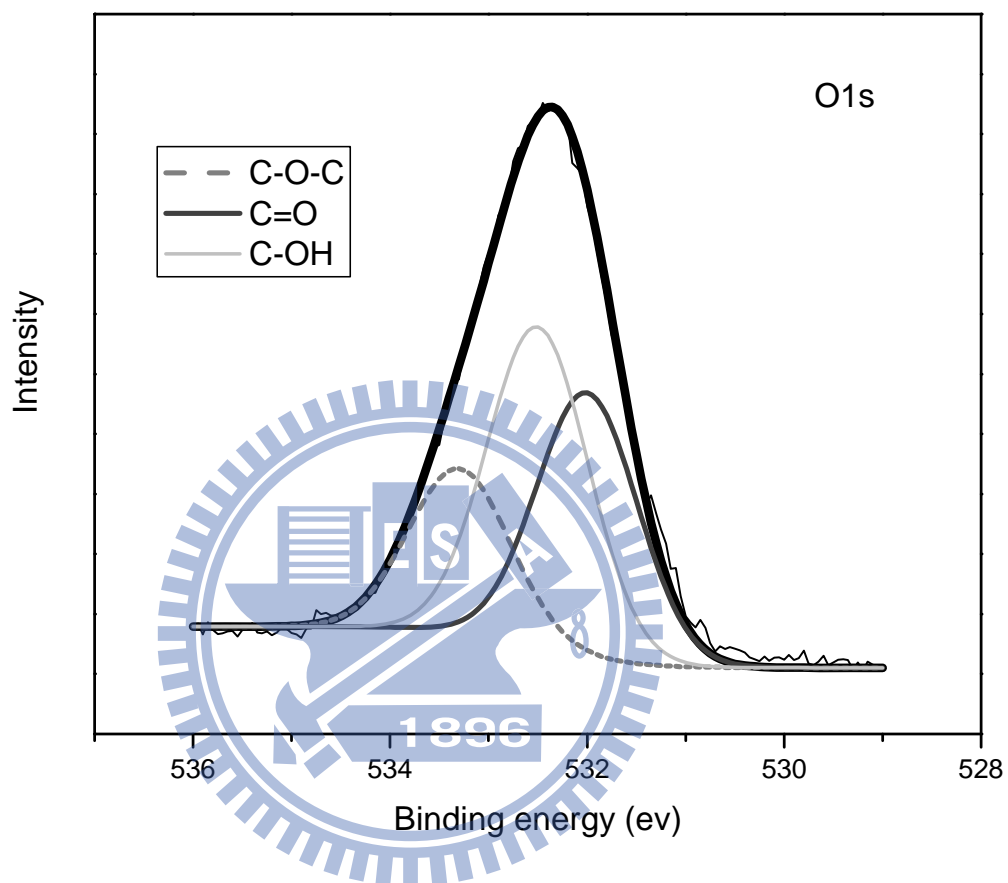


Figure 4. 8. The XPS O1s spectra of ODPA-BADB polyimide films oxygen plasma treated at 50W RF Power, time treatment for 5mins

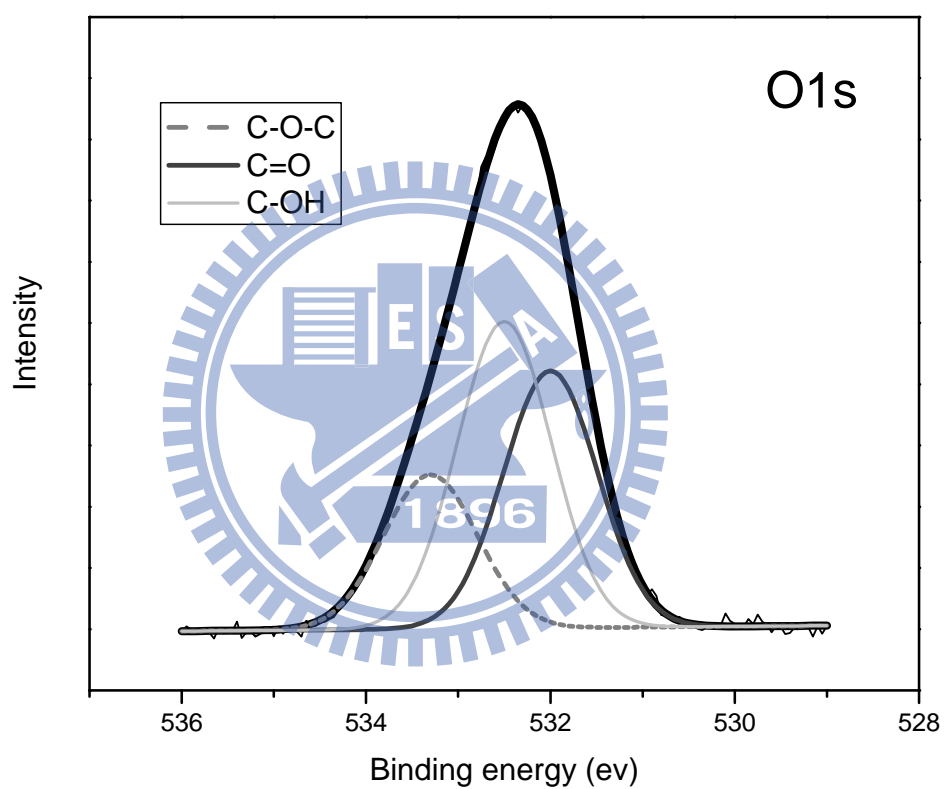
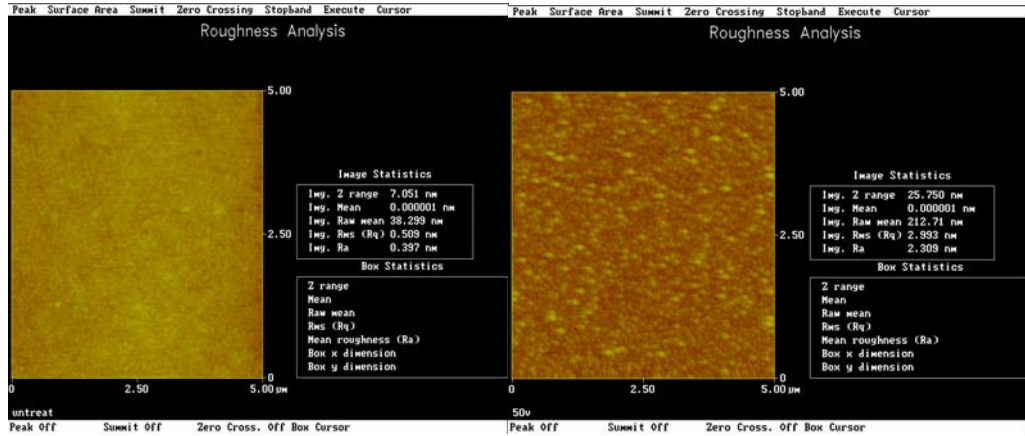


Figure 4. 9. The XPS O1s spectra of ODPA-BADB polyimide films oxygen plasma treated at 100W RF Power, time treatment for 5mins

4.2 Surface Morphology and Roughness of PI by Using AFM

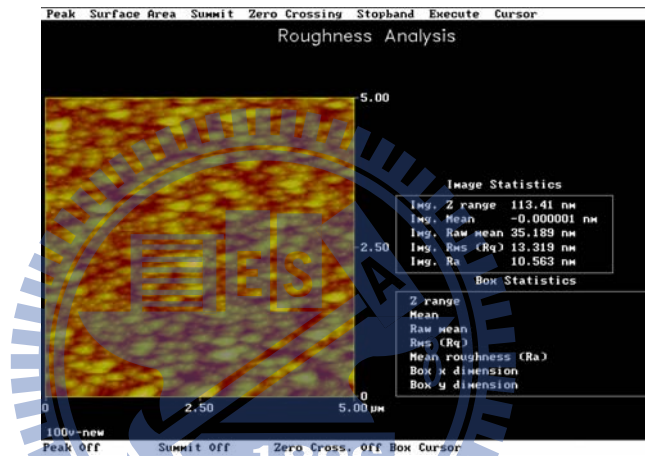
Figures 4.10 and 4.11 show the surface morphologies of ODPA-BADB polyimide as-prepared and after oxygen plasma treatment at 50 W and 100 W for 5 minutes. The root-mean-square (RMS) roughness of the PI increased with the increasing RF power. RMS roughness of PI was increased from 0.509 nm prior to plasma treatment to 2.993 nm using 50 W treatment, and 13.319 nm using 100 W treatment.





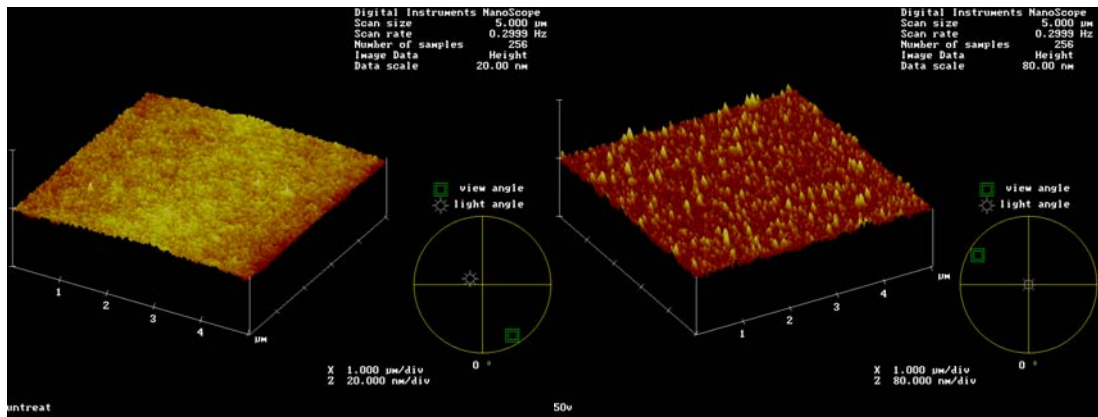
(a)

(b)



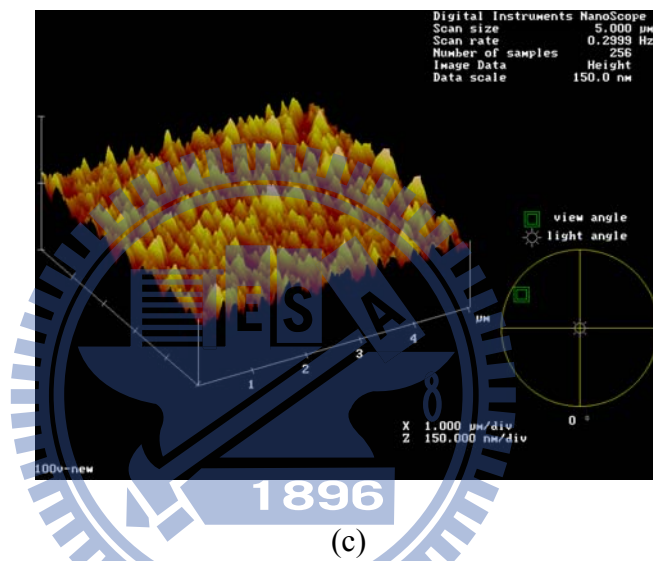
(c)

Figure 4. 10. The AFM two-dimensional images of the PI surface: (a) as-prepared (untreated), (b) oxygen plasma treatment at 50 W for 5 mins, (c) oxygen plasma treatment at 100 W for 5 mins



(a)

(b)



(c)

Figure 4. 11. The AFM three-dimensional images of the PI surface: (a) as-prepared (untreated), (b) oxygen plasma treatment at 50 W for 5 mins, (c) oxygen plasma treatment at 100 W for 5 mins

4.3 Surface Energy of ODP A-BADB Polyimide

The water contact angle of the PI samples was determined before and after the oxygen plasma treatment. The surface energy on PI treated with oxygen plasma at different plasma power and treatment time is determined by Equation (3.3) and is summarized in Table 4.10. Each sample was measured at three random points. Based on the data in Table 4.10, the average surface energy of PI films with and without oxygen plasma treatment are listed in Table 4.11. The result showed that the surface energy increased significantly after plasma treatment from 27.9 to 125-131 mN/m for various treatment power and time. Only slight increase in surface energy (from 125 to 131 mN/m) was observed when higher power or longer treatment time was used in the oxygen plasma treatment.

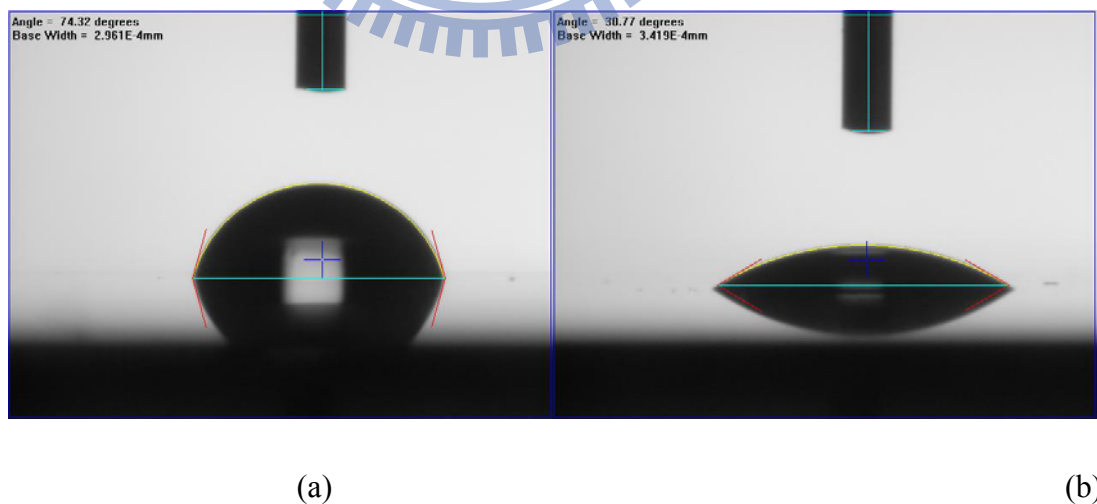


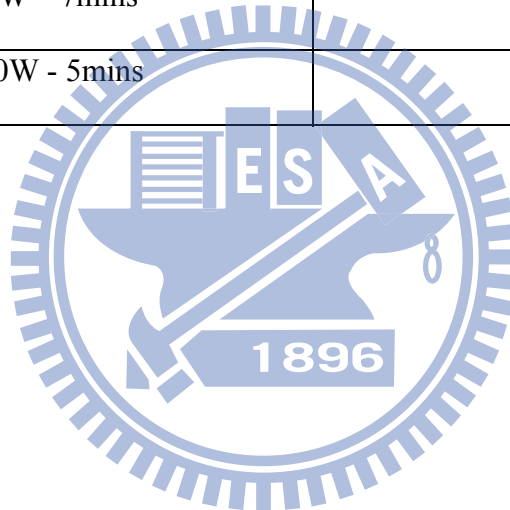
Figure 4. 12. The images of contact angle for (a) untreated PI surface and (b) oxygen plasma modified PI surface

Table 4. 10. The contact angle, wetting tension, and surface energy of PI surface with and without oxygen plasma treatment (raw data)

Condition treatment	Contact angle (deg)	Wetting tension (dyne/cm)	Surface energy (mN/m)
Untreated	79.78	12.96	25.73
	74.32	11.43	30.89
	78.16	12.33	27.1
50W - 1min	29.87	63.3	125.7
	29.43	63.58	126.28
	30.77	62.73	124.59
50W – 3mins	30.94	62.62	124.37
	30.20	63.09	129.32
	31.04	62.55	124.24
50 W – 5 mins	30.21	63.09	125.31
	29.31	63.65	126.43
	29.35	63.63	126.39
50W – 7mins	27.73	64.61	128.34
	29.56	63.5	126.13
	26.36	65.41	129.92
100W – 5mins	24.68	66.33	131.75
	25.09	66.11	131.32
	26.37	65.4	129.9

Table 4. 11. The surface energy of PI surface with and without oxygen plasma treatment

Sample	Surface energy (mN/m)
Untreated	27.91 ± 1.99
50W – 1 min	125.52 ± 0.62
50W – 3mins	125.98 ± 2.23
50W – 5mins	126.04 ± 0.49
50W – 7mins	128.13 ± 1.33
100W - 5mins	130.99 ± 0.73



4.4 Adhesion of AZO/PI Interface

4.4.1 Control of the AZO Film Thickness on Polyimide

The deposition conditions of AZO onto PI film have been described in Table 3.3. The thickness of AZO was measured by SEM images. It was found that the growth rate was constant at 3.64 nm/min. Therefore, a deposition time of 55 minutes was used in order to obtain a 200 nm thickness AZO film on the polyimide film. A cross-sectional SEM viewgraph of AZO film on PI was illustrated in Figure 4.13

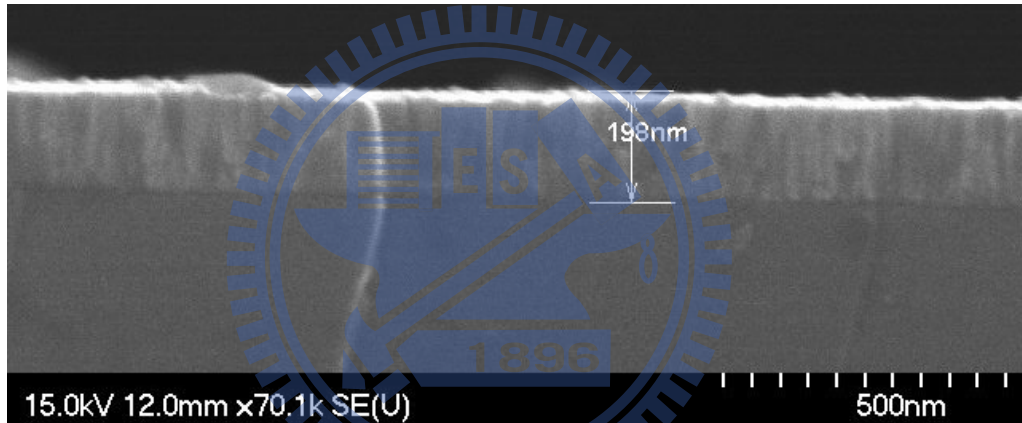
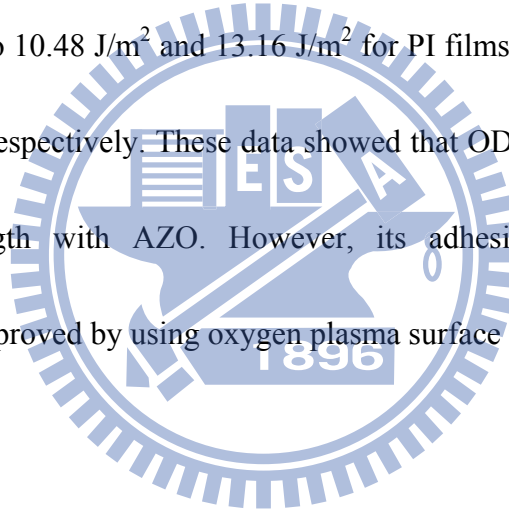


Figure 4. 13. SEM image of a 200 nm thick AZO film on polyimide

4.4.2 Adhesion Energy of AZO/PI Interface

The adhesion energy between AZO and PI were measured by using four point bending test. The critical load P_c for a specific sample was obtained from the load – displacement curve as illustrated in Figure 4.14. The adhesion energy was then calculated by using Equation 3.1. Figure 4.15 shows the fractured interfaces (PI surface and AZO surface) or possible cohesion failure after four point bending test.

The fractured interface can be readily confirmed by a simple multi-meter based on their difference in the electric conduction. In this measurement, the average adhesion data was obtained from 4 samples with valid fractured interface at AZO/PI. The average adhesion strength of AZO/PI interface for as-prepared PI and oxygen plasma modified PI using different RF power and treatment time were summarized in Table 4.13. The adhesion energies of AZO/PI interface increased with increasing RF power for PI surface modification. The adhesion energy was 5.31 J/m^2 for untreated PI, but was increased to 10.48 J/m^2 and 13.16 J/m^2 for PI films treated with oxygen plasma at 50 and 100W, respectively. These data showed that ODPA-BADB polyimide had low adhesion strength with AZO. However, its adhesive strength with AZO was significantly improved by using oxygen plasma surface modification of polyimide.



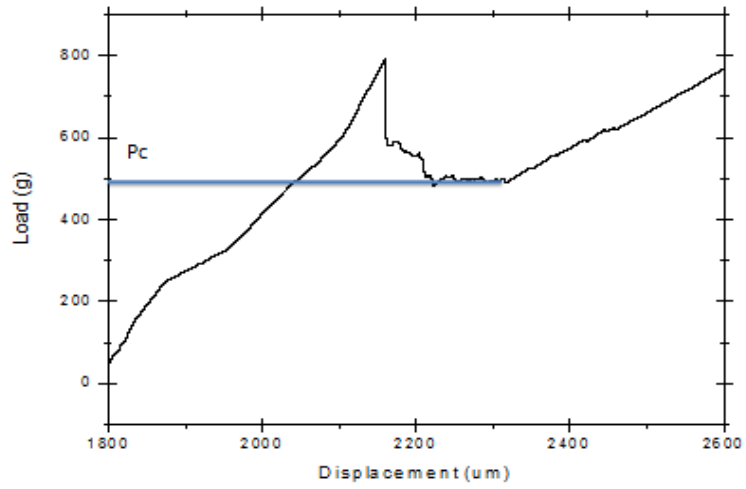


Figure 4. 14. A load vs. displacement curve of a AZO/PI sample under four point bending test

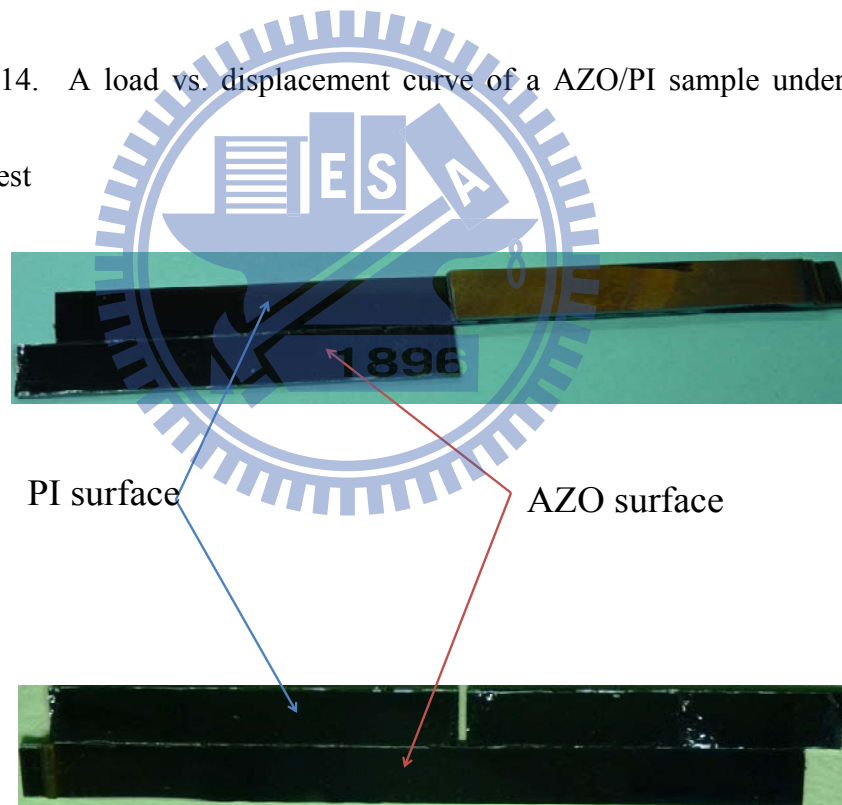


Figure 4. 15. Photographs of polyimide and AZO after fracture under four point bending test

Table 4. 12. The critical loads and adhesion strength of AZO/PI interface for PI with and without oxygen plasma treatment with different RF power.

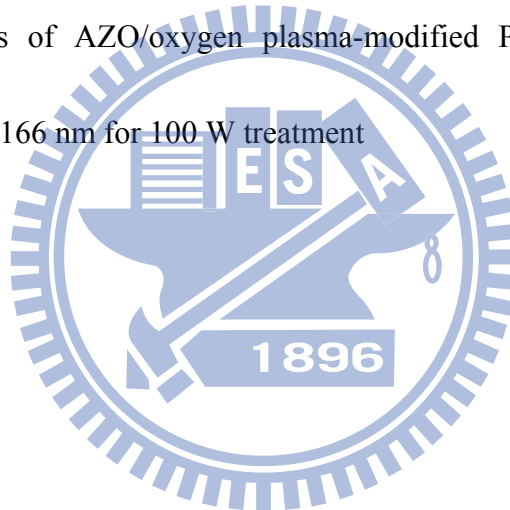
sample	Critical load (g)	Adhesion strength (J/m ²)
Untreated	495	6.36
	458	5.44
	445	5.14
	475	4.28
50 W	604	9.47
	664	11.44
	631	10.33
	641	10.66
100 W	694	12.5
	708	13
	726	13.68
	720	13.45

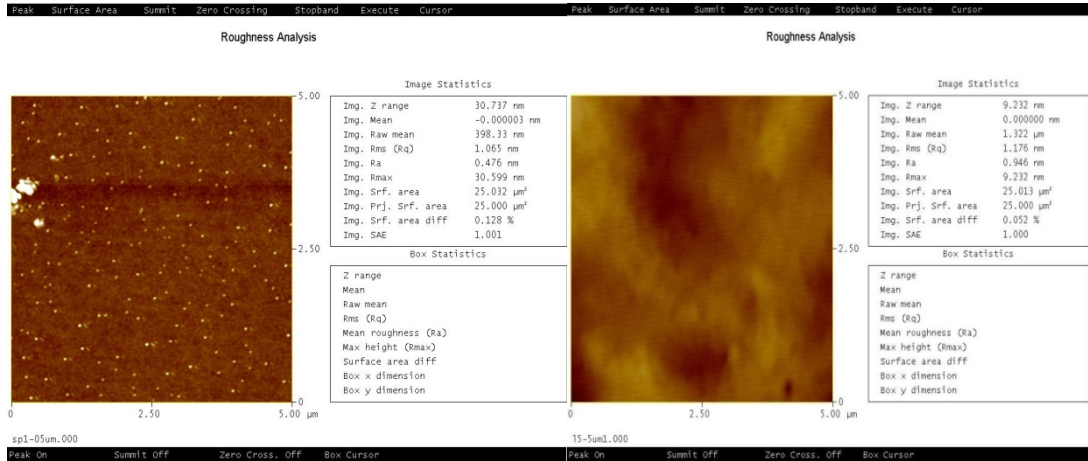
Table 4. 13. The average values of adhesion energy AZO/PI interface for PI with and without oxygen plasma treatment

Sample	Gc (J/m ²)
Untreated	5.31 ± 0.60
50W	10.48 ± 0.58
100W	13.16 ± 0.41

4.5 Surface Roughness of AZO/PI Using AFM

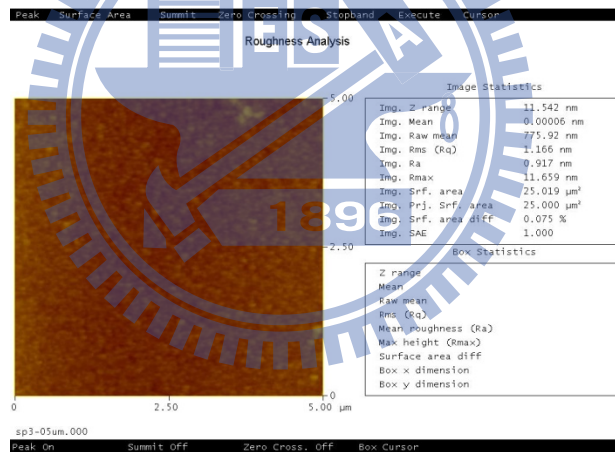
Figure 4.16 and Figure 4.17 show the surface morphology of AZO grown on untreated PI and oxygen plasma treated PI at 50W and 100W for 5 minutes. The surface of AZO was very smooth, although AZO was deposited onto PI with roughness ranging from 0.509 nm for as-prepared PI as shown in Figure 4.10 to 2.993-12.319 nm for PI modified by oxygen plasma at 50 and 100 W shown in Figure 4.11. It was found that the RMS roughness of AZO/untreated PI was 1.065nm. And the RMS roughness of AZO/oxygen plasma-modified PI was 1.176 nm for 50 W treatment and 1.166 nm for 100 W treatment





(a)

(b)



(c)

Figure 4.16. The AFM two-dimensional images of AZO surfaces deposited on polyimide(a) untreated, (b) modified by oxygen plasma at 50W, and (c) modified by oxygen plasma at 100 W.

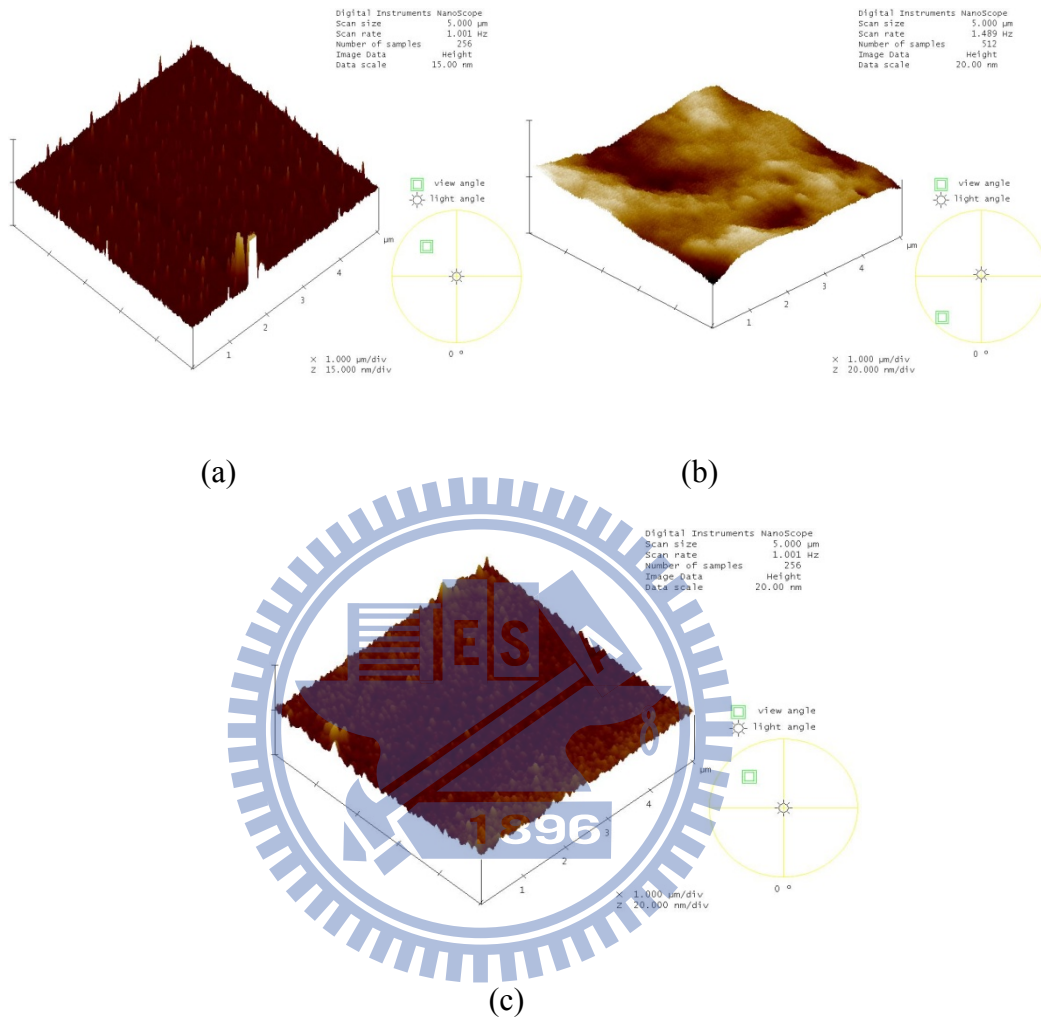


Figure 4.17. The AFM three-dimension images of AZO surfaces deposited on polyimide (a) untreated, (b) modified by oxygen plasma at 50W, and (c) modified by oxygen plasma at 100 W.

4.6 XRD of AZO Film Deposited on Polyimide

Figure 4.18 shows XRD patterns of the AZO films deposited on the untreated PI and oxygen plasma modified PI substrates. A symmetrical (0002) peak (near 34.5°) from the ZnO layer was observed, while no metallic Zn or Al characteristic peaks were found. After oxygen plasma treatment, the intensity of AZO peaks increased slightly. The average grain size were calculated by using Equation 2.2 and summarized in Table 4.14. The grain size increased slightly from 50 nm to 52-53 nm when PI surface was modified by oxygen plasma treatment. The grain size increase due to the formation of polar groups.

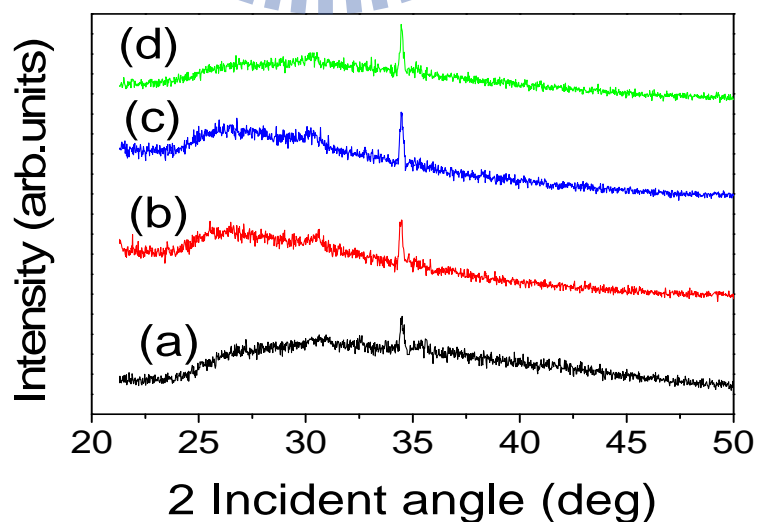
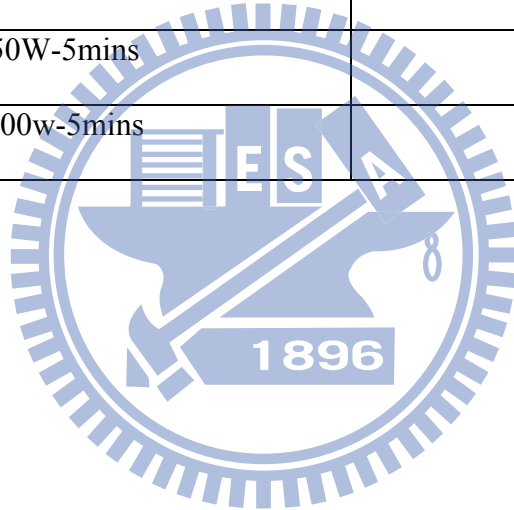


Figure 4. 18. XRD patterns of AZO thin films deposited on (a) untreated PI (b) PI treated by oxygen plasma at 50W for 1 minutes (c) PI treated by oxygen plasma at 50W for 5 minutes, and (d) PI treated by oxygen plasma at 100W for 5 minutes

Table 4. 14. The average grain size of AZO deposited on untreated PI and oxygen plasma modified PI.

Sample	Grain size (nm)
Untreated	50.0
50W-1min	53.4
50W-5mins	52.1
100w-5mins	52.9



4.7 Resistivity of AZO Deposited on Polyimide

Table 4.15 lists the resistivity of AZO deposited on PI before and after oxygen plasma treatment. The resistivity of AZO onto untreated PI was $2.05 \times 10^{-3} \Omega\text{cm}$. The resistivity of AZO was increased to $2.75 \times 10^{-3} \Omega\text{cm}$ and $3.75 \times 10^{-3} \Omega\text{cm}$ for PI film treated by oxygen plasma at 50 W for 1 and 5 mins, respectively. The resistivity of AZO increased more double when AZO was deposited onto PI treated at 100W for 5 minutes.

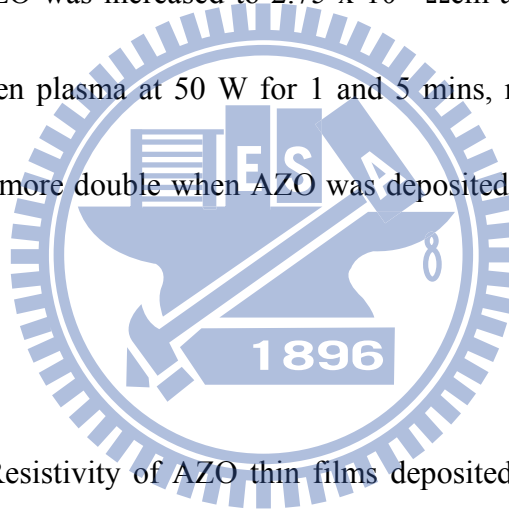


Table 4. 15. Resistivity of AZO thin films deposited on polyimide films with and without oxygen plasma modification

Sample	Resistivity (Ωcm)
Untreated	2.05×10^{-3}
50W-1min	2.75×10^{-3}
50W-5mins	3.75×10^{-3}
100w-5mins	4.61×10^{-3}

4.8 Discussion

4.8.1 Modification of ODPA-BADB Polyimide Surface Chemical State

Binding energies and composition quantification of polyimide as obtained by XPS C1s and O1s spectra are summarized in Table 4.16. The modification of PI surface could be explained by the reaction mechanisms schematically described in Figure 4.19. The reaction mechanisms [70-72] were proposed based on their bonding energies and quantification listed in Table 4.13.

Reaction 1: The C-O-C was broken into two parts. One was to form a new group C-OH and the other to form a carbonyl group, inducing C-O-C bond to a C=O bond.

Reaction 2: The C-N bond was broken and led to an increase of C-OH group.

Reaction 3: The alkyl group was broken to form C-OH bond. Therefore, the component ratio of C-C group decreased while the component ratio of C-OH group increased.

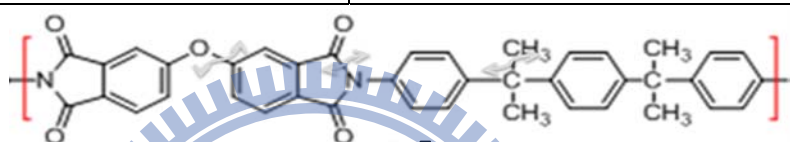
In the C1s spectra, the component of C-C was decreased after oxygen plasma treatment as explained in Reaction 3. The new group, C-OH was formed and increased due to the C-C bonds were broken. The chain scission of C-O-C bond was more difficultly than C-N bond and C-C bond due to their corresponding bonding energy. The C-O-C is 351 KJ/mole while C-N bond energy is 305 KJ/mole and C-C bond energy is 347 KJ/mole.

In the O1s signal, the component ratio of C-O-C and C=O decreased due to Reaction 1 and Reaction 2. After these bonds were broken, the new group C-OH was formed and its relative percentage increased from 0% to 42.53%,42.75% and 42.7%. These results presented the surface chemical states of polyimide films had modified by oxygen plasma treatment.

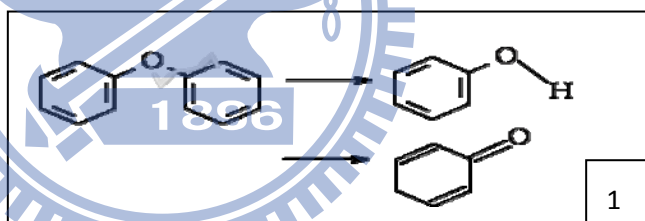


Table 4. 16. Binding energies of typical chemical bonds.

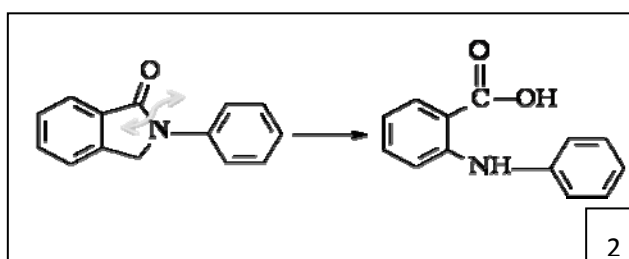
Bond	Bond energy (KJ/mole)
C-N	305
C-C	347
C-O	351
C-H	411
C-C in benzene	446
C=O	620



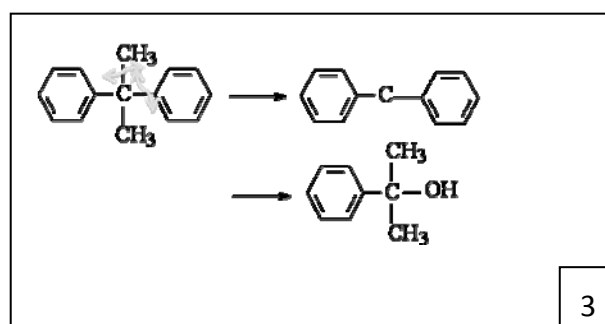
: The structure was broken
by oxygen plasma



1



2



3

Figure 4. 19. Proposed surface reaction mechanisms in ODPA-BADB polyimide surface modified by oxygen plasma treatment.

Table 4. 17. Binding energies (eV) and composition quantification (%) of ODPA-BADB polyimide as obtained by XPS C1s and O1s spectra.

Component	C1s				O1s			
	As received (eV)	Plasma treated			As received (eV)	Plasma treated		
		50W 1min	50W 5min	100W 5min		50W 1min	50W 5min	100W 5min
C-C	284.8 (83.58%)	284.8 (45.43%)	284.8 (46.32%)	284.8 (46.55%)				
C-O-C	285.8 (10.08%)	285.8 (19.5%)	285.8 (18.13%)	285.8 (18.84%)	533.3 (41.1%)	533.3 (20.8%)	533.3 (21.45%)	533.3 (21.9%)
C=O	288.6 (6.34%)	288.6 (13.95%)	288.6 (13.55%)	288.6 (12.65%)	532 (58.9%)	532 (36.67%)	532 (35.8%)	532 (35.4%)
C-OH		287.3 (21.12%)	287.3 (22%)	287.3 (21.96%)		532.5 (42.53%)	532.5 (42.75%)	532.5 (42.7%)

4.8.2 Surface Chemical States Affect on Surface Energy of ODPA-BADB Polyimide

The surface energy of PI increases significantly after using oxygen plasma treatment. Furthermore, it is independent of power and treatment time showed in Figure 4.20 and 4.21. After plasma treatment polymer, implantation of special elements such as oxygen leads to reactions with polymer surface and thus new polar

groups such as C-OH, C-O-C, C=O. Thus, such formation of the polar group can account for the increase of surface energy after plasma treatment. [73,74,75] The surface energy of PI after treatment was independent with power and treatment time. This was consistent with our XPS analysis that the surface composition quantification of PI film modified by oxygen plasma was also independence of power and treatment time.

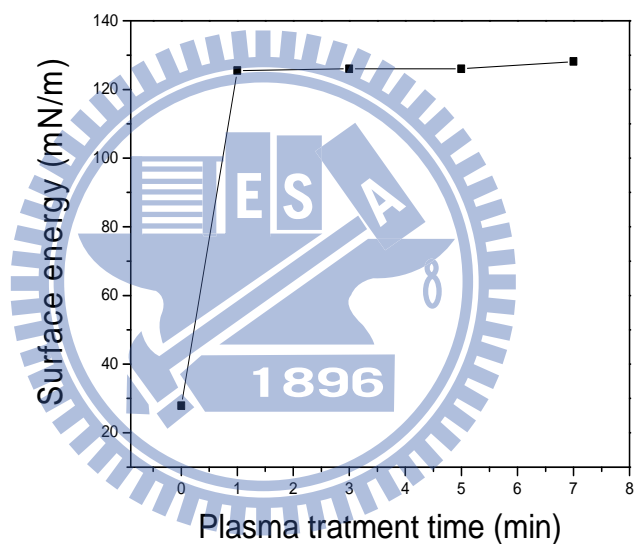


Figure 4. 20. Surface energy of PI films untreated and oxygen plasma treated for various times at a power of 50W

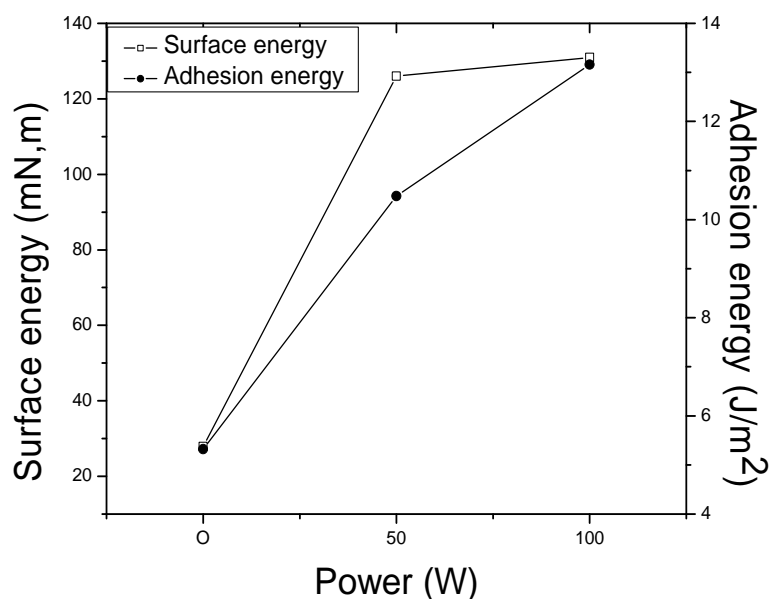


Figure 4. 21. Surface energy on PI and adhesion energy of AZO/PI interface for PI films untreated and oxygen plasma treated using different power at a fixed 5-min treatment time

4.5.3 Effects of Surface Chemical States and Roughness on the Adhesion of AZO/PI Interface

The adhesion increased with increasing treatment power due to composition quantification of PI film modified by oxygen plasma and increasing surface roughness.

After plasma treatment, the percentage of polar groups such as C=O, C-O-C increased.

In addition, a new polar group, C-OH was observed.

The results showed that both the surface energy of PI and adhesion energy of AZO/PI increased significantly after PI was treated by oxygen plasma. Adhesion energy increased with the increasing of RF treatment power, but the surface energy of PI increased slightly with increasing power and treatment time. The enhanced adhesion at AZO/PI interface can be attributed to increased roughness [76] and the formation of the new polar group such as C-OH and increased percentage of oxygenated, polar groups such as C-O and C=O on PI surface.

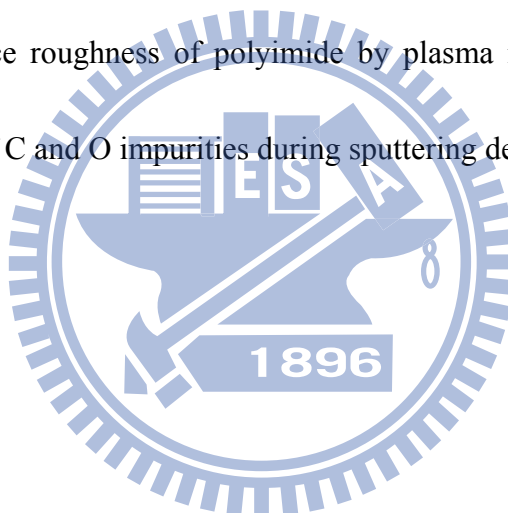
4.5.6 Surface Modification of ODPA-BADB Polyimide Affect on Electrical Property of AZO

The XRD result showed that the crystallinity of AZO and the grain size increased slightly. Yet, this has negligible effect on the resistivity. The roughness of PI surface significantly increased after oxygen plasma treatment. The RMS roughness of PI increased from 0.509nm for as-prepared PI, to 3.607 nm and 13.319 for PI treated by oxygen plasma at 50W and 100 W, respectively. The rough interface of substrate and thin films may contribute to electron scattering and thus to the film electrical conductivity. The increased resistivity of AZO/PI can be attributed to the increased surface roughness of polyimide after plasma surface modification[77] .

Chapter 5 Conclusions

Our attentions focused on the building block, AZO/PI substrate stacking for various flexible devices such as flexible OLEDs and flexible solar cells. The adhesion strength of AZO/PI interface was investigated in order to improve the reliability of such building block for the flexible device. Oxygen plasma treatment was used to modify the surface of polyimide. The surface chemical states of polyimide before and after plasma treatment were characterized by X-ray photoelectron spectroscopy (XPS). The component ratio of polar groups as C-O-O, C=O, and new C-OH surface functionality increased after oxygen plasma treatment, but independence of the conditions of plasma treatment. The polyimide surfaces morphology was measured by atomic force microscope (AFM). The AFM images showed the roughness of the polyimide surface increased with increasing RF power in the oxygen plasma treatment. The surface energy of PI film was calculated by using contact angle measurement. The surface energy increased significantly after plasma treatment from 27.9 to 125-131 mN/m for various treatment power and time. Only slight increase in surface energy (from 125 to 131 mN/m) was observed when higher power or longer treatment time was used. The results showed that both the surface energy of PI and adhesion energy of AZO/PI increased significantly after PI was treated by oxygen plasma. Adhesion energy increased with the increasing of RF treatment power, but the surface energy of

PI increased slightly with increasing power and treatment time. The enhanced adhesion at AZO/PI interface can be attributed to increased roughness and the formation of the new polar group such as C-OH and increased percentage of oxygenated, polar groups such as C-O and C=O on PI surface. The surface of AZO remained very smooth when deposited onto oxygen plasma-modified polyimide films. However, the resistivity of AZO film degraded if polyimide film was treated by oxygen plasma. The increased resistivity of AZO films can be attributed to the increased surface roughness of polyimide by plasma modification and possibly the incorporation of C and O impurities during sputtering deposition.



References

- [1] H. L. Hartnagel, A. L. Dawar, A. K. Jain, and C. Jagadish, *Semiconducting Transparent Thin Films* Institute of Physics, (1995).
- [2] Man Gu Kang, Nam-Gyu Park, Kwang Sun Ryu, Soon Ho Chang and Kang-Jin Kim. *Solar Energy Materials and Solar Cells*. 90 (2006) 574
- [3] H. Kim, J. S. Horwitz, G. P. Kushto, Z. H. Kafafi, and D. B. Chrisey. *Appl. Phys. Lett.* 79 (2001) 284
- [4] F. X. Qiu, Y. M. Zhou, and J. Z. Liu, *Eur. Polym. J.* 40 (2004) 713.
- [5] P. C. Chiang and W. T. Whang, *Polymer* 44, (2003) 2249.
- [6] Ka Eun Lee, Mingsong Wang, Eui Jung Kim, and Sung Hong Hahn, *Appl. Phys.* 9 (2009) 683
- [7] Chang S. Moon, Yun M. Chung, Woo S. Jung, Jeon G. Han, *Surf. Coat. Technol.*, 201 (2007) 5035
- [8] R. Nakh Wong, Toemsak Srihirin, Tanakorn Osotchan, *Advanced Materials Research*, 55-57,(2008), 753
- [9] Stephen J. Pearton, and David P. Norton, *Plasma Process. Polym.* 2(2005)16
- [10] S. Guruvenket, G. Mohan Raoa, Manoj Komath, Ashok M. Raichur, *Appl. Surf. Sci.* 236 (2004) 278

- [11] S.Y. Xiao, L.F. Che, X.X. Li, and Y.L. Wang, *Microelectronic Engineering* 85 (2008) 452
- [12] Sarah Han, *Flexible display technology and market*, displaybank (2007)
- [13] Gerwin Gelinck, Paul Heremans, Kazumasa Nomoto, and Thomas D. Anthopoulos, *Adv. Mater.* 22 (2010)3778
- [14] Ralf Dunkel, Roko Bujas, Andre Klein, and Volker Horndt, *Proceedings of the IEEE* 93(2005)8
- [15] Z.Y. Xie, Y.Q. Li, F.L. Wong, and L.S. Hung, *Materials Science and Engineering* 106 (2004) 219
- [16] Mark Dai Joong Auch , Ong Kian Soo, Guenther Ewald and Chua Soo-Jin, *Thin solid films*, 417 (2002) 47
- [17] Yasuyuki Watanabe, Hiroyuki Iechi, and Kazuhiro Kudo *Jpn. J. Appl. Phys.* 45 (2006) 3698
- [18] Lee-Ching Kuo, Yu-Tai Tsai, Wen-Yueh Hsu and Neng-Hsing Lu, *Photovoltaic Energy Conversion*, 1 (1994) 690
- [19] Jay Lewis, *Material Today*, 9 (2006) 4
- [20] H. Ito, W. Oka, H. Goto, and H. Umeda, *Jpn. J. Appl. Phys.* 45, (2006),4325
- [21] G. Dennler, C. Lungenschmied , H. Neugebauer , N.S. Sariciftci , M. Latre`che , G. Czeremuszkin, M.R. Wertheimer, *Thin Solid Films* 511 – 512 (2006) 349

- [22] J.S. Lewis, M.S. Weaver, IEEE J. Sel. Top. Quantum Electron. 10 (2004) 45
- [23] Myeon-Cheon Choi, Youngkyoo Kim, and Chang-Sik Ha Prog. Polym. Sci. 33 (2008) 581
- [24] Hutchinson, J. W., and Suo, Z., Adv. Appl. Mech. , 63 (1992) 29
- [25] A. Onur Sergici Nicholas, X. Randall, Advantage Material & Processes (2006)
- [26] K. W. Wong, L. Y. Sin, M. K. Yeung, S. K. Hark, R. X. Du, W. M. Lau, Appl. Phys. A 87, (2007) 23
- [27] Elmoursi, Alaa A.; Patel, Nilesh, J. Adhesion Sci. Technol. 18 (2004) 597
- [28] S.H.Lau, Elie Tolentino, Yuen Lim, Evangeline Tolentino and Ann Koo, Journal of Electronic materials 30 (2001)299
- [29] S. R. Hosseini, N. Choupani, and A. R. M. Gharabaghi, International Journal of Mechanical, Industrial and Aerospace Engineering 2(2008)4
- [30] Qing Ma, J. Mater. Res,12,(1997)3
- [31] S.G. Zhenghao Gan, Mhaisalkar, Zhong Chen, Sam Zhang, Zhe Chen, K. Prasad, Surface & Coatings Technology 198 (2005) 85
- [32] M.Strobel, C, Lyons,and K.L Mittal, Plasma surface modification (1994) 231
- [33] F. D. Egitto, L.J. Matienzo, IBMJ.Res.Develop, 38 (1994) 4
- [34] Ching-Yu Yang, J. S. Chen and Steve Lien-Chung Hsu, J. Electrochem. Soc 153 (2006)120

- [35] Y. Nakamura, Y. Suzuki, Y. Watanabe, Thin Solid Film 290 (1996) 367
- [36] R. Daniel, Kammler, O. Thomas, Mason, and R Kenneth. Poepelmeier, J. Am. Ceram. Soc, 84 (2001) 1004
- [37] Tadatsugu Minami, Semicond. Sci. Technol. 20 (2005) 35
- [38] Cathleen A. Hoel, Thomas O. Mason, Jean-Franc-ois Gaillard, and Kenneth R. Poepelmeier, Chem. Mater, 22 (2010), 3569
- [39] Sonja Hartner, Moazzam Ali, Christof Schulz, Markus Winterer and Hartmut Wiggers. Nanotechnology 20 (2009) 445701
- [40] Jong-Pil Kim, Sang-A Lee, Jong Seong Bae, Sung-Kyun Park, Ung-Chan Choi, Chae-Ryong Cho, Thin Solid Films, 516 (2008) 5223
- [41] S.H. Mohamed, A.M. Abd El-Rahman, A.M. Salem, L. Pichon, F.M. El-Hossary, Journal of Physics and Chemistry of Solids, 67 (2006) 2351
- [42] N. H. Thomson, Journal of Microscopy, 217 (2005) 193
- [43] Sam Hu in Nano Interconnect & Packaging Laboratory (NIP Lab) unpublished data.
- [44] M. Damayanti, J. Widodo, T. Sritharan, S.G. Mhaisalkar, W. Lu, Z.H. Gan, K.Y. Zeng, L.C. Hsia. B 121 (2005) 193
- [45] S.J. Howard, A.J. Phillipps, and T.W. Clynn. Fatigue and Fracture of Inorganic Composites. 24 (1993) 103

- [46] Nathan Cheung, U.C. Berkeley in Department of Electrical Engineering and
Computer Sciences of University of California at Berkeley
- [47] E.D. Wolf, I. Adesida, and J.D.Chinn, J.Vac. Sci.Technol, 2(1984)2
- [48] Henri Janseny, Han Gardeniers, Meint de Boer, Miko Elwenspoek and Jan
Fluitman, J. Micromech. Microeng. 6 (1996) 14
- [49] C. C. Chang, Surf. Sci. 25 (1971) 53
- [50] David Echevarría Torres, University of Texas at El Paso College of Science
Chemistry Department
- [51] Abdulaziz, in Material Science Program of Washington State University
- [52] R. W. M. Kwok, Ph. D. Dissertation: Fabrication of InP MISFET. Canada:
Western University of Ontario, 1993
- [53] Henriette Estrade-Szwarckopf, Carbon 42 (2004) 1713
- [54] F. M. Nakhei and A. Bahari, Int. J. Phys. Sci. 4 (2009) 290
- [55] Marius Enachescu et al. Environmental AFM and SPFM Results
- [56] J. C. González, M. I. N. da Silva, K. L. Bunker, and P.E. Russell, Scanning
Microscopy and Scanning Electron Microscopy (2004)
- [57] Phil Russell, Dale Batchelor in College of Engineering North Carolina State
University

- [58] Roger P. Woodward, A New Dynamic Contact Angle System, (1995)
- [59] N. K. Adam, Nature , 180 (1957) 809
- [60] Miao Ju Chuang, Surf. Coat. Technol 203 (2009) 3527
- [61] Derrick O. Njobuenwu, Esio O. Oboho, Rhoda H.Gumus, Leonardo Electronic
Journal of Practices and Technologies,6, (2007) 28
- [62] D. McMullan, Cavendish Laboratory, University of Cambridge, UK (1993)
- [63] Judith A Smith, Phys. Educ. 17 (1982), 111
- [64] Daniel Jädernäs, Linköping University, IFM, April 2007
- [65] Standard Operation Procedure of four point bending system, NIP lab, National
Chiao Tung University
- [66] Andrew P. Schuetze, Wayne Lewis, Chris Brown, and Wilhelmus J. Geerts, Am. J.
Phys. 72 (2004) 149
- [67] G. Beamson and D. Briggs, Chichester 184 (1992)
- [68] D. Wolany, T. Fladung, L. Duda, and J. W. Lee, Surf. Interface Anal. 27 (1999)
609
- [69] M. P. Hughey, D. J. Morris, R. F. Cook ,S. P. Bozeman , B. L. Kelly , S. L. N.
Chakravarty, D. P. Harkens , and L. C. Stearns, Eng. Fract. Mech. 7 (2004) 245
- [70] T. L. Cottrell, The Strengths of Chemical Bonds, 2nd ed. (Butterworth Scientific,
London, (1958).

- [71] B. Darwent, National Bureau of Standard, Washington, DC, 1970.
- [72] S. Benson, J. Chem. Educ. 42 (1965),502
- [73] W.J. Park, S.G. Yoon, W.S. Jung and D.H. Yoon, Surf. Coat. Technol, 201
(2007) 5017
- [74] I. A. Rusu, G. Popa, S.O. Aaied, J. I. Sullivan, Journal of Optoelectronics and
Advanced Materials 8 (2006) 1935
- [75] B.M.P. Ferreira, L.M.P. Pinheiro, P.A.P. Nascente, M.J. M.J. Ferreira and E.A.R.
Duek, C 29 (2009) 806
- [76] Soo Hong Kim, Sun Woong Na, N.-E. Lee, Yun Woo Nam, Young-Ho Kim,
Surf. Coat. Technol, 200 (2005) 2072
- [77] Prater, W. L.; Allen, E. L.; Lee, W.-Y.; Toney, M. F.; Kellock, A.; Daniels,
J. S.; Hedstrom, J. A.; Harrell, T. Journal of Applied Physics, 97(2005)
093301